

# A SPECTRAL METHOD FOR HALF-INTEGER SPIN FIELDS BASED ON SPIN-WEIGHTED SPHERICAL HARMONICS

FLORIAN BEYER, BORIS DASZUTA, AND JÖRG FRAUENDIENER

ABSTRACT. We present a new spectral scheme for analysing functions of half-integer spin-weight on the 2-sphere and demonstrate the stability and convergence properties of our implementation. The dynamical evolution of the Dirac equation on a manifold with spatial topology of  $\mathbb{S}^2$  with a pseudo-spectral method is also demonstrated.

## 1. INTRODUCTION

In a recent paper [3] we presented a spectral method for tensorial partial differential equations on geometries with a spherical component. We showed how to implement the ‘eth’-formalism based on spin-weighted spherical harmonics following the work by Newman, Penrose and others [9, 23]. The restriction to tensorial equations implied the use of spin-weighted functions with integer spin-weights. In the present work we extend our method to also include functions with half-integer spin-weight on spherical geometries. In particular, we show how the evolution of dynamical half-integer spin fields can be accomplished. Our motivation for doing so stems mainly from General Relativity: spinorial fields describing elementary particles such as electrons or neutrinos are fundamental sources for the Einstein equations and are studied for instance as test fields on Kerr-Newman backgrounds, see [10] and references therein. However, there are also interesting developments in condensed matter physics in relation to the description of graphene [5, 39] for which our method might be relevant. The numerical treatment of the Dirac field is particularly interesting as its evolution can be rather peculiar and sometimes even counter-intuitive as visualised by Thaller [34, 35].

It is well known that when working with  $\mathbb{S}^2$  (and other compact geometries) coordinate singularities can lead to instabilities that spoil the accuracy of numerical schemes. These issues can be avoided by working with spectral methods where coordinate-independent manipulation of expressions in terms of a well-defined basis of functions upon which the action of differential operators reduces to algebraic manipulation is possible [4, 11]. Thus, issues of coordinate singularities are dealt with automatically by the method.

Our spectral method makes use of the spin-weighted spherical harmonics (SWSH) [9, 23, 25, 26] which can be shown to be equivalent to the well-known Wigner  $D$ -functions [6, 29, 33] and thus provide a complete, orthonormal basis for  $L^2(SU(2))$ . In the description of half-integer spin fields, we have found it convenient to work directly with the half-integer SWSH due to the particularly simple action of the associated  $\bar{\delta}$  and  $\bar{\delta}'$  differential operators which may be thought of as constituting covariant derivative operators on the sphere [9]. As the action of the aforementioned operators on the SWSH reduces to simple algebraic manipulation we may translate PDE systems into coupled (infinite dimensional) ODE systems and thus construct a spectral evolution scheme for an initial value problem (IVP) of interest.

Our work extends that of [3,15] into a spectral algorithm for spin-weighted spherical harmonics (SWSH) with half-integer spin-weight  $s$ . The method we present inherits several desirable properties from [3,15]. In particular it is theoretically exact if a minimum number of grid points are used at a given band-limit  $L$ . Furthermore the same algorithmic complexity of  $\mathcal{O}(L^3)$  is achievable for spectral transformations. In brief, [3,15] seek to calculate values for the integer SWSH over  $\mathbb{S}^2$  by mapping the sphere into the 2-torus (thus allowing for Fast Fourier Transforms to be used) and relate the SWSH to the reduced Wigner  $d$ -functions evaluated at  $\pi/2$ . For a short summary of past work related to the integer case see [3]. The approach to the half-integer case is in principle similar, however suitable modification of the 2-torus map must be made in order to account for the periodicity of spinor fields. In addition, the recursion relation [36] that allows for evaluation of the Wigner  $d$ -functions must be modified.

As a toy model we numerically explore the dynamics associated with a Dirac equation on a 2-dimensional manifold with spatial topology of  $\mathbb{S}^2$  as an IVP. This will allow for a test of the spin-weighted spectral transformations we present in the context of evolution equations. Common techniques for treating the numerical problem of the Dirac equation consist of: FD schemes formulated on a flat-lattice in configuration space [12,13], on a grid within a finite-volume in momentum-space [22] and using methods based on the split-step operator technique [7,8,20,21]. Particular to the FD approach special care must be taken so as to avoid the Fermion-doubling problem [24]. Elimination of spurious modes introduced to the solution may be accomplished by means of nonlocal approximation for the spatial derivative operator [32,38] or by staggered-grid schemes [12,13]. As remarked upon in [13] the issue of spurious modes is not particular to the Dirac equation but can occur whenever a symmetric FD approximant is used for a first derivative on a uniform grid. We seek to avoid the above issue entirely by making use of the global approximation to functions and derivative operators that spectral methods provide [14].

The equations of motion (EOM) that we derive for the Dirac equation in the aforementioned geometric setting result in a coupled system of variable-coefficient linear hyperbolic PDEs. When performing a SWSH decomposition this results in product terms that must be further simplified. From past experience [3] we have found that while it is possible to make use of Clebsch-Gordan expansions (see sec. 2), i.e., working entirely in the space of coefficients, it is far more convenient to instead work with a pseudo-spectral method (see sec. 5.1), and thus we follow the latter approach in this work.

This paper is structured as follows: In sec. 2 we recall basic properties of the half-integer SWSH together with the  $\mathfrak{d}$ -formalism. In sec. 2.1 and 2.2 respectively we discuss the forward and backward spectral transformations of spin-weighted functions on the sphere. In sec. 3 we present the required modification to the recursion relation for computing the reduced Wigner functions at  $\pi/2$ . Subsequently, in sec. 4 we perform consistency checks on our implementation of the algorithm. Error pairs and the property of exponential convergence are analysed. In sec. 5 we proceed by numerically solving the 2 + 1 dimensional Dirac equation as an IVP on a curved geometry, specifying to cases with spatial topology of  $\mathbb{S}^2$ . We find EOM adapted to the spin-weighted formalism. In sec. 5.1 we briefly recall the pseudo-spectral method. In sec. 5.2 we construct numerical solutions to the EOM and inspect convergence properties of the numerical solutions obtained together with conserved currents. Sec. 6 concludes.

## 2. SWSH SUMMARY

In this section we briefly summarise key properties of the spin-weighted spherical harmonics (SWSH) that we will make use of in the presentation of our half-integer spectral algorithm and in the pseudo-spectral method for solution of dynamical systems. For further details we refer the reader to [3, 6, 9, 23, 25, 26].

Geometrically, the spin-weighted functions are sections of certain line bundles over the 2-sphere  $\mathbb{S}^2$ . They have a representation in terms of ordinary functions over patches of  $\mathbb{S}^2$  which depend on the choice of coordinates and the choice of an orthonormal frame at points of the patch. The behaviour of this representation under changes of the frame is captured by the spin-weight assigned to the function. Here, we will deal only with representations of the spin-weighted functions given in terms of the standard polar coordinates  $(\vartheta, \varphi)$  and the orthonormal frame defined in terms of the coordinate derivative vectors

$$e_\vartheta = \partial_\vartheta, \quad e_\varphi = \frac{1}{\sin \vartheta} \partial_\varphi. \quad (2.1)$$

Equivalently, these vectors can be obtained as real and imaginary parts of the complex linear combination

$$m = \frac{1}{\sqrt{2}} (e_\vartheta - ie_\varphi) = \frac{1}{\sqrt{2}} \left( \partial_\vartheta - \frac{i}{\sin \vartheta} \partial_\varphi \right)$$

which, together with its complex conjugate, satisfies the orthonormality relations

$$m \cdot m = 0, \quad \bar{m} \cdot \bar{m} = 0, \quad m \cdot \bar{m} = 1$$

at all points of  $\mathbb{S}^2$  covered by the polar coordinates with respect to the standard metric on  $\mathbb{S}^2$ .

Every smooth function  ${}_s f$  on  $\mathbb{S}^2$  with spin-weight  $s$  can be expressed as:

$${}_s f(\vartheta, \varphi) = \lim_{L \rightarrow \infty} \sum_{l=|s|}^L \sum_{m=-l}^l {}_s a_{lm} {}_s Y_{lm}(\vartheta, \varphi), \quad (2.2)$$

where the  ${}_s Y_{lm}$  are the SWSH, which form a complete orthonormal basis for the complex vector space of spin-weight  $s$  functions.

Recall that the action of the  $\bar{\partial}$  and  $\partial'$  differential operators on  ${}_s f$  serves to raise and lower the spin-weight respectively; when viewed as maps with respect to polar coordinates we have:

$$\bar{\partial} : {}_s f \rightarrow {}_{s+1} \tilde{f}, \quad \bar{\partial} [{}_s f] = \partial_\vartheta [{}_s f] - i \csc \vartheta \partial_\varphi [{}_s f] - s \cot \vartheta {}_s f, \quad (2.3)$$

$$\partial' : {}_s f \rightarrow {}_{s-1} \tilde{f}, \quad \partial' [{}_s f] = \partial_\vartheta [{}_s f] + i \csc \vartheta \partial_\varphi [{}_s f] + s \cot \vartheta {}_s f. \quad (2.4)$$

The SWSH may be written explicitly as:

$${}_s Y_{lm}(\vartheta, \varphi) = \sqrt{\frac{2l+1}{4\pi}} \exp(im\varphi) d_{sm}^l(\vartheta), \quad (2.5)$$

where  $d_{mn}^l(\vartheta)$  is the reduced Wigner  $d$ -function:

$$d_{mn}^l(\vartheta) = \sum_{r=\max(0, m-n)}^{\min(l+m, l-n)} (-1)^{r-m+n} \frac{\sqrt{(l+m)!(l-m)!(l+n)!(l-n)!}}{r!(l+m-r)!(l-r-n)!(r-m+n)!} \times \\ \times \cos^{2l-2r+m-n} \left( \frac{\vartheta}{2} \right) \sin^{2r-m+n} \left( \frac{\vartheta}{2} \right). \quad (2.6)$$

Under complex conjugation the SWSH satisfy:

$$\overline{{}_s Y_{lm}} = (-1)^{s-m} {}_{-s} Y_{l, -m} \iff {}_s Y_{lm} = (-1)^{s-m} \overline{{}_{-s} Y_{l, -m}}. \quad (2.7)$$

The SWSH satisfy the orthonormality relation:

$$\langle {}_s Y_{l_1 m_1}, {}_s Y_{l_2 m_2} \rangle = \int_0^{2\pi} \int_0^\pi {}_s Y_{l_1 m_1}(\vartheta, \varphi) \overline{{}_s Y_{l_2 m_2}(\vartheta, \varphi)} \sin \vartheta \, d\vartheta \, d\varphi = \delta_{l_1 l_2} \delta_{m_1 m_2}. \quad (2.8)$$

A particularly useful property the SWSH possess is that under the action of  $\bar{\partial}$  and  $\bar{\partial}'$  the action of Eq. (2.3) and Eq. (2.4) reduces to a "ladder algebra":

$$\bar{\partial} [{}_s Y_{lm}(\vartheta, \varphi)] = -\sqrt{(l-s)(l+s+1)} {}_{s+1} Y_{lm}(\vartheta, \varphi), \quad (2.9)$$

$$\bar{\partial}' [{}_s Y_{lm}(\vartheta, \varphi)] = \sqrt{(l+s)(l-s+1)} {}_{s-1} Y_{lm}(\vartheta, \varphi), \quad (2.10)$$

which we will exploit when performing decompositions of dynamical equations, allowing for a map from a PDE system to an (infinite dimensional) ODE system (see sec. 5). In addition to this we have the commutator expression:

$$[\bar{\partial}, \bar{\partial}'] {}_s Y_{lm}(\vartheta, \varphi) = -2s {}_s Y_{lm}(\vartheta, \varphi). \quad (2.11)$$

A product of two SWSH with spin-weights  $s_1$  and  $s_2$  is a function of spin-weight  $s_1 + s_2$  and, therefore, it can be written as a finite linear combination of SWSH

$${}_s Y_{l_1, m_1}(\vartheta, \varphi) {}_{s_2} Y_{l_2, m_2}(\vartheta, \varphi) = \sum_{l \in \Lambda'} \mathcal{C}_l(s_1, l_1, m_1; s_2, l_2, m_2) {}_{(s_1+s_2)} Y_{l, (m_1+m_2)}(\vartheta, \varphi), \quad (2.12)$$

where  $\Lambda' := \{\max(|l_1 - l_2|, |s_1 + s_2|, |m_1 + m_2|), \dots, l_1 + l_2\}$  and the coefficients are related to the usual Clebsch-Gordan coefficients, see e.g. [3, 29].

**2.1. Forward transformation.** We now describe our numerical algorithm for evaluation of the forward transform  $\mathcal{F} : {}_s f \mapsto ({}_s a_{lm})$ . As a first step we introduce the notation  $\Delta_{mn}^l := d_{mn}^l(\pi/2)$  which allows for the rewriting of Eq. (2.6) as [28]:

$$d_{mn}^l(\vartheta) = i^{m-n} \sum_{q=-l}^l \Delta_{qm}^l e^{-iq\vartheta} \Delta_{qn}^l, \quad (2.13)$$

following from a factoring of rotations [36]. In particular, note that  $d_{mn}^l(\vartheta) = \overline{d_{mn}^l(\vartheta)}$  (cf. Eq. (2.6)). We defer the details of how the  $\Delta$  elements are calculated together with their symmetry properties to sec. 3.

Define the functional:

$$I_{mn} [{}_s f(\vartheta, \varphi)] := \int_0^{2\pi} \int_0^\pi e^{-im\vartheta} e^{-in\varphi} {}_s f(\vartheta, \varphi) \sin \vartheta \, d\vartheta \, d\varphi. \quad (2.14)$$

This integral can be evaluated exactly – we now describe our method which is based on [15]. Combining eqs. (2.2), (2.5), (2.13) and (2.14) results in:

$${}_s a_{lm} = i^{s-m} \sqrt{\frac{2l+1}{4\pi}} \sum_{q=-l}^l \Delta_{qs}^l I_{qm} \Delta_{qm}^l, \quad (2.15)$$

$$= i^{s-m} \sqrt{\frac{2l+1}{4\pi}} \sum_{q=1/2}^l \Delta_{qs}^l J_{qm} \Delta_{qm}^l, \quad (2.16)$$

where

$$J_{qm} := I_{qm} + (-1)^{2l+s+m} I_{-q, m}. \quad (2.17)$$

In order to make use of existing FFT (fast Fourier transform) algorithms in the evaluation of the quadrature in Eq. (2.14), we must extend a spin-weighted function  ${}_s f$  with data sampled on the domain  $D := \{(\vartheta, \varphi) | \vartheta \in [0, \pi], \varphi \in [0, 2\pi]\}$  to a  $4\pi$  periodic function on  $\tilde{D} := \{(\vartheta, \varphi) | \vartheta \in [0, 4\pi], \varphi \in [0, 4\pi]\}$ . This is accomplished using the intrinsic symmetries of the  ${}_s Y_{lm}(\vartheta, \varphi)$  together with the expansion ansatz of Eq. (2.2). For convenience we define the domains  $D_I, \dots, D_{\text{VIII}}$  (see Fig. 1).

We have  $D = D_I$  upon which  ${}_s f(\vartheta, \varphi) = {}_s f_I(\vartheta, \varphi)$ . For  $D_{II}$  put  ${}_s f_{II}(\vartheta, \varphi) =$

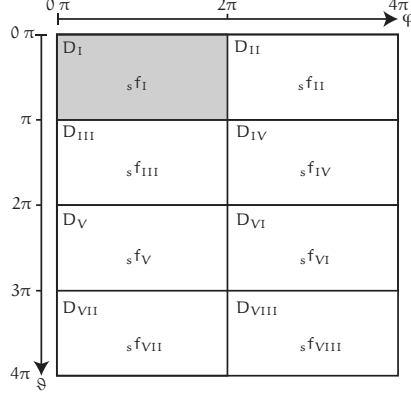


FIGURE 1. Domains for function extension. The shaded region corresponds to data that are to be extended to unshaded regions.

${}_s f_I(\vartheta, \varphi - 2\pi)$ . Next, define  ${}_s g : D_I \cup D_{II} \rightarrow \mathbb{C}$  by

$${}_s g(\vartheta, \varphi) := \begin{cases} {}_s f_I(\vartheta, \varphi) & (\vartheta, \varphi) \in D_I \\ {}_s f_{II}(\vartheta, \varphi) & (\vartheta, \varphi) \in D_{II} \end{cases}. \quad (2.18)$$

Now, define  ${}_s h : D_I \cup D_{II} \cup D_{III} \cup D_{IV} \rightarrow \mathbb{C}$  by

$${}_s h(\vartheta, \varphi) := \begin{cases} {}_s g(\vartheta, \varphi) & (\vartheta, \varphi) \in D_I \cup D_{II} \\ (-1)^{s+1} {}_s g(2\pi - \vartheta, (\varphi - \pi) \bmod 4\pi) & (\vartheta, \varphi) \in D_{III} \cup D_{IV} \end{cases} \quad (2.19)$$

Finally, we arrive at the extended function  ${}_s F : \tilde{D} \rightarrow \mathbb{C}$  defined by

$${}_s F(\vartheta, \varphi) := \begin{cases} {}_s h(\vartheta, \varphi) & (\vartheta, \varphi) \in D_I \cup D_{II} \cup D_{III} \cup D_{IV} \\ -{}_s h(\vartheta - 2\pi, \varphi) & (\vartheta, \varphi) \in D_V \cup D_{VI} \cup D_{VII} \cup D_{VIII} \end{cases} \quad (2.20)$$

The smooth function  ${}_s F(\vartheta, \varphi)$  is  $4\pi$  periodic in  $\vartheta$  and  $\varphi$ , thus we may write:

$${}_s F(\vartheta, \varphi) = \sum_{k=0}^K \sum_{m=0}^M {}_s F_{km} e^{ik\frac{2\pi}{4\pi}\vartheta} e^{im\frac{2\pi}{4\pi}\varphi}. \quad (2.21)$$

In order to evaluate (2.14) we now identify

$$I_{mn} [{}_s f(\vartheta, \varphi)] \equiv I_{mn} [{}_s F(\vartheta, \varphi)] = \int_0^{2\pi} \int_0^\pi e^{-im\vartheta/2} e^{-in\varphi/2} {}_s F(\vartheta, \varphi) \sin \vartheta \, d\vartheta d\varphi, \quad (2.22)$$

where we can extend the indices to all integers, i.e.,  $m, n \in \mathbb{Z}$ . This is permissible as both functions are equal in the region of integration. Upon substitution with Eq. (2.21) we find:

$$I_{mn} [{}_s F(\vartheta, \varphi)] = \sum_{i,j=0} {}_s F_{ij} W_\vartheta(i-m) W_\varphi(j-n), \quad (2.23)$$

with

$$W_\vartheta(\tau) := \int_0^\pi e^{i\tau\vartheta/2} \sin \vartheta \, d\vartheta = \begin{cases} \pm i \frac{\pi}{2} & \tau = \pm 2 \\ 4 \frac{1+i\tau}{4-\tau^2} & \tau \in \mathbb{Z} \setminus \{\pm 2\} \end{cases}, \quad (2.24)$$

$$W_\varphi(\rho) := \int_0^{2\pi} e^{i\rho\varphi/2} d\varphi = \begin{cases} 2\pi & \rho = 0 \\ \frac{2i}{\rho} (1 - (-1)^\rho) & \rho \in \mathbb{Z} \setminus \{0\} \end{cases}. \quad (2.25)$$

Equation (2.23) amounts to a two-fold discrete convolution in spectral space. By the convolution theorem, this implies that we may equivalently consider pointwise multiplication of the inverse transforms of  $W_\vartheta$  and  $W_\varphi$  with  ${}_sF$ . Let  $N_\vartheta$  and  $N_\varphi$  denote the number of grid points over  $\vartheta$  and  $\varphi$  on the containerization of  $\mathbb{S}^2$  that the function  ${}_sf(\vartheta, \varphi)$  is to be sampled at. Upon extension to the doubly  $4\pi$  periodic domain (see Fig. 1) we work instead with the extended function  ${}_sF(\vartheta, \varphi)$ . Furthermore, in order to simplify numerical construction of the extension, the number of samples on the extended domain is taken to be  $N'_\vartheta = 4N_\vartheta - 3$  and  $N'_\varphi = 2N_\varphi - 1$ . Correspondingly, the spatial sampling intervals are now given by  $\Delta\vartheta = \frac{4\pi}{N'_\vartheta-1}$  and  $\Delta\varphi = \frac{4\pi}{N'_\varphi-1}$ . In order to satisfy the Nyquist condition, such that spurious aliasing does not occur, we impose  $N_\vartheta = N_\varphi = 2(L + 2 - 1/2) + 1$ , where  $L$  is the harmonic that the function  ${}_sf(\vartheta, \varphi)$  is band-limited to<sup>1</sup>.

Under these choices a convenient form of the quantities discussed above that is directly amenable to numerical work is given by:

$$\tilde{W}_\vartheta(\gamma) := \sum_{\delta=0}^{N'_\vartheta-2} e^{i\gamma\delta\Delta\vartheta/2} W_\vartheta \left( \frac{N'_\vartheta-1}{2} - \delta \right) \quad \gamma = 0, \dots, N'_\vartheta - 2 \quad (2.26)$$

$$\tilde{W}_\varphi(\varepsilon) := \sum_{\zeta=0}^{N'_\varphi-2} e^{i\varepsilon\zeta\Delta\varphi/2} W_\varphi \left( \frac{N'_\varphi-1}{2} - \zeta \right) \quad \varepsilon = 0, \dots, N'_\varphi - 2 \quad (2.27)$$

together with:

$$I_{\mu\nu} [{}_sF(\vartheta, \varphi)] = \frac{1}{(N'_\vartheta-1)(N'_\varphi-1)} \sum_{\gamma=0}^{N'_\vartheta-2} \sum_{\varepsilon=0}^{N'_\varphi-2} e^{-i\mu\gamma\Delta\vartheta/2} e^{-i\nu\varepsilon\Delta\varphi/2} \times \tilde{W}_\vartheta(\gamma)\tilde{W}_\varphi(\varepsilon) {}_sF(\gamma, \varepsilon). \quad (2.28)$$

where  $\mu \in 0, \dots, N'_\vartheta - 2$ ,  $\nu \in \{0, \dots, N'_\varphi - 2\}$ . Note that in this approach, we must discard all values of  $I_{\mu\nu}$  for which  $\mu$  and  $\nu$  are even integers. In order to recover  $I_{mn}$  from Eq.(2.28) we take  $\mu = \frac{1}{2}(N'_\vartheta - 4m - 1)$  and  $\nu = \frac{1}{2}(N'_\varphi - 4n - 1)$ . Overall we find an algorithmic complexity of  $\mathcal{O}(L^3)$  as the integrals  $I_{\mu\nu}$  may be evaluated exactly in  $\mathcal{O}(L^2 \log L)$  operations by performing a two-dimensional FFT and each component of  $\Delta_{mn}^l$  (as required by Eq. (2.16)) can be computed using  $\mathcal{O}(1)$  floating point evaluations – see sec. 3 and also [15, 36]. We remark that if the analysis of strictly real data is desired then it is possible to attain a linear increase in the execution speed of transformations (specifically the FFT component by a factor of approximately 2). However, as we are primarily interested in applying transformations for the solution of equations of motions that govern the dynamics of complex fields we do not explore this further.

**2.2. Backward transformation.** We now describe the algorithm for evaluation of the backward (inverse) transform  $\mathcal{F}^{-1} : ({}_sa_{lm}) \mapsto {}_sf$ . The backward spherical harmonic transform maps the expansion coefficients  ${}_sa_{lm}$ , for  $|s| \leq l \leq L$ , to a function on (a dense subset of)  $\mathbb{S}^2$ . Because we are working with band-limited functions we can, at the analytical level, perfectly reconstruct the original function. To this end, Eq. (2.2) must be evaluated. As the inverse transform does not contain

<sup>1</sup> More efficient samplings on the sphere may be possible [19] however the overall asymptotic complexity of our proposed algorithm will not be affected and thus we do not explore this issue here.

integrals, issues of quadrature accuracy do not arise. Define:

$$K_{mn} [{}_s a_{ln}] := i^{s-n} \sum_{l=|s|}^L \sqrt{\frac{2l+1}{4\pi}} \Delta_{-m,ss}^l a_{ln} \Delta_{-m,n}^l \quad (2.29)$$

which allows for:

$${}_s f(\vartheta, \varphi) = \sum_{m=-\frac{1}{2}(N'_\vartheta-1)+\frac{1}{2}}^{\frac{1}{2}(N'_\vartheta-1)-\frac{1}{2}} \sum_{n=-\frac{1}{2}(N'_\varphi-1)+\frac{1}{2}}^{\frac{1}{2}(N'_\varphi-1)-\frac{1}{2}} e^{im\vartheta} e^{in\varphi} K_{mn}. \quad (2.30)$$

Use of Eq. (3.1) permits a rewriting of Eq. (2.30) as:

$$K_{mn} [{}_s a_{ln}] = \begin{cases} i^{s-n} \sum_{l=|s|}^L \sqrt{\frac{2l+1}{4\pi}} \Delta_{-m,ss}^l a_{ln} \Delta_{-m,n}^l & m \geq \frac{1}{2} \\ i^{s-n} \sum_{l=|s|}^L \sqrt{\frac{2l+1}{4\pi}} (-1)^{2l+s+n} \Delta_{m,ss}^l a_{ln} \Delta_{m,n}^l & m \leq -\frac{1}{2} \end{cases}, \quad (2.31)$$

which allows for a reduction in computation time. In Eq. (2.30) we may use an FFT directly, discarding values of  ${}_s f(\vartheta, \varphi)$  for which  $\vartheta > \pi$  and  $\varphi > 2\pi$ . If the input data to the FFT library is Hermitean then another linear increase ( $\sim 2$ ) in the execution speed of a transform is possible however, this again does not change the overall algorithmic complexity  $\mathcal{O}(L^3)$ .

### 3. WIGNER $\Delta$ AND RECURSION

Here we answer the question of how to compute the  $\Delta_{mn}^l$  required in the forward and backward transforms. We will base our numerical algorithm for computation of an arbitrary  $\Delta_{mn}^l$  on recursion and exploitation of symmetries.

First we note the symmetry properties (inherited from  $d_{mn}^l(\vartheta)$ ):

$$\Delta_{-m,n}^l = (-1)^{l+n} \Delta_{mn}^l \quad (3.1)$$

$$\Delta_{m,-n}^l = (-1)^{l-m} \Delta_{mn}^l \quad (3.2)$$

$$\Delta_{mn}^l = (-1)^{n-m} \Delta_{nm}^l. \quad (3.3)$$

Using an approach similar to [36] one can derive an analogous Trapani-Navaza (TN) style recursion from Eq. (2.6) for half-integer  $l, m, n$  values:

$$\Delta_{ll}^l = \frac{1}{2} \Delta_{l-1,l-1}^{l-1} \quad (3.4)$$

$$\Delta_{ml}^l = \sqrt{\frac{l(2l-1)}{2(l+m)(l+m-1)}} \Delta_{m-1,l-1}^{l-1} \quad (3.5)$$

$$\Delta_{mn}^l = m \sqrt{\frac{2}{l}} \Delta_{m,n+1}^l \quad (n = l-1) \quad (3.6)$$

$$\Delta_{mn}^l = \frac{2m}{\sqrt{(l-n)(l+n+1)}} \Delta_{m,n+1}^l - \sqrt{\frac{(l-n-1)(l+n+2)}{(l-n)(l+n+1)}} \Delta_{m,n+2}^l \quad (|n| \leq l-2) \quad (3.7)$$

$$\Delta_{l,\frac{1}{2}}^l = \sqrt{\frac{2l}{2l+1}} \Delta_{l-1,\frac{1}{2}}^{l-1} \quad (3.8)$$

Note that by making use of the symmetries provided by eqs. (3.1)–(3.3) similar recursion relations may be constructed connecting different combinations of subscript indices.

We visualise the possible values of  $\Delta_{mn}^l$  up to some maximal band-limit  $L$  as being arranged in a square pyramidal lattice with  $\Delta_{mn}^l$  values corresponding to

$l = 1/2$  and  $-1/2 \leq m, n \leq 1/2$  occupying the top-most plane;  $l = 3/2$  and  $-3/2 \leq m, n \leq 3/2$  the next plane down and so forth. In a recursive approach one can thus initialise with a single value of  $\Delta_{mn}^{1/2}$  and with eqs. (3.4), (3.5) and (3.8) (together with symmetries) compute those values of  $\Delta_{mn}^l$  constrained to the surface of the pyramidal lattice. For each fixed  $l$  value those  $\Delta_{mn}^l$  that occupy the interior of the pyramidal structure can be computed using Eq.(3.6) and Eq.(3.7) (together with symmetries).

We note that symmetries allow for a reduction in the total number of elements that must be calculated explicitly via recursion to  $((2l+1)/2)^2$  entries for a fixed  $l$  plane and  $\frac{1}{12}(2L+3)(2L+1)(L+1)$  total entries for a choice of maximal band-limit  $L$ .

In our implementation we initialise with  $\Delta_{1/2,-1/2}^{1/2} = 1/\sqrt{2}$  and iterate such that for a given  $l$  the  $m, n$  indices obey the condition  $(n < 1/2) \wedge (|m| \geq |n|) \wedge (m > -1/2)$ .

Working with double precision arithmetic, we have found that the above scheme remains stable up to a band-limit of  $L \approx 5173/2$ . Due to exponential convergence [4] this  $L$  will in practical situations be far above the resolution required to accurately sample fields for evolution equations and thus is not a concern for this work. We note however, that by instead working with ratios such as  ${}_r\Delta_{mn}^l = \Delta_{mn}^l / \Delta_{m-1,n}^l$  we have verified that it is possible to construct a stable type of hybrid recursion in analogy to [3], for  $L > 5173/2$ .

#### 4. SWSH CONSISTENCY CHECKS

As a first check on the consistency of the half-integer SWSH algorithm presented above we construct error pairs. Here one populates coefficients with random data whereupon a transformation is applied so as to construct the spatial representation of the corresponding function; this spatial function is transformed back to coefficients and the associated error may be examined. This procedure may be summarised as:

$${}_s\tilde{a}_{lm} \xrightarrow{\mathcal{F}^{-1}} {}_s f(\vartheta, \varphi) \xrightarrow{\mathcal{F}} {}_s\tilde{a}_{lm}, \quad (4.1)$$

The real and imaginary parts of  ${}_s\tilde{a}_{lm}$  we generate by sampling from the continuous uniform random distribution on the interval  $[-1, 1)$ . The numerical error associated with the specification of Eq. (4.1) is shown in Fig. 2(a) and Fig. 2(b). We see that our implementation is indeed consistent, accurate and stable. Furthermore the scaling  $L(n)$  of  $\epsilon_{\text{rel rms}}$  (Fig. 2(b)) for the half-integer spin-weight uniform random data matches the scaling observed for integer spin-weight Gaussian random data observed in [15].

The product of two spin-weighted functions  ${}_{s_1}f$  and  ${}_{s_2}g$  on  $\mathbb{S}^2$  is a function with spin-weight  $s_1 + s_2$ . If  ${}_{s_1}f$  and  ${}_{s_2}g$  are comprised of a finite number of SWSH then their product is also and thus by selecting a sufficiently large  $L$  we exactly sample the resulting product function. We can also check the property of exponential convergence; to this end define  $A_l := \langle {}_s a_{lm} \rangle_m = \sum_m |{}_s a_{lm}| / (2l+1)$ , a measure of the average magnitude of coefficients at a fixed  $l$  value. We expect that given smooth test functions  $A_l$  should behave as  $A_l \sim \alpha \exp(-\kappa l)$  ( $\alpha, \kappa \in \mathbb{R}$ ) for large  $l$  [4, 16]. Smooth half-integer spin-weighted functions may be constructed by taking

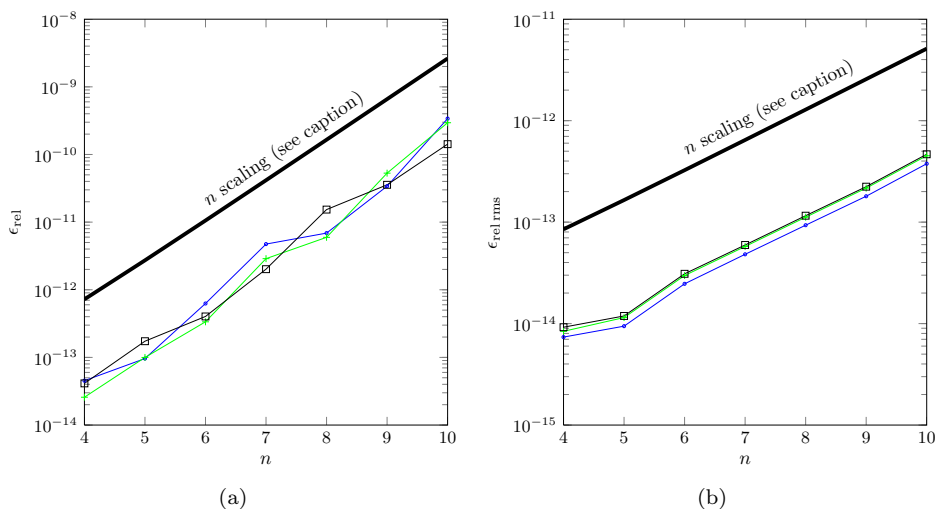


FIGURE 2. (Colour online) Averages of numerical error pairs when performing the transform procedure of Eq. (4.1). A fixed spin-weight  $s$  is chosen and 5 sets of  ${}_s a_{lm}$  are randomly generated as described in the text. In both sub-figures the band-limit of transforms is given by  $L(n) = (2^n - 1)/2$ . (a) Averaged maximum, absolute relative error  $\epsilon_{\text{rel}} := \langle \max_{l,m} |1 - {}_s \tilde{a}_{lm} / {}_s \tilde{\alpha}_{lm}| \rangle$ . The thick black line corresponds to a scaling of  $L(n)^2$ . (b) Averaged maximum, absolute relative rms error  $\epsilon_{\text{rel,rms}} := \langle \langle {}_s \tilde{a}_{lm} - {}_s \tilde{\alpha}_{lm} \rangle_{\text{rms}} / \langle {}_s \tilde{a}_{lm} \rangle_{\text{rms}} \rangle$ . The thick black line corresponds to a scaling of  $L(n)$ . In (a) and (b): Green "+" corresponds to  $s = 3/2$ ; blue "o" corresponds to  $s = 13/2$ ; black "□" corresponds to  $s = -1/2$ .

a finite number of SWSH and modulating by the exponential of a smooth spin-weight 0 function. Introduce:

$${}_0 g(\vartheta, \varphi) = i {}_0 Y_{3,-1}(\vartheta, \varphi) + 1.1 {}_0 Y_{3,1}(\vartheta, \varphi) \quad (4.2)$$

$${}_0 \tilde{g}(\vartheta, \varphi) = \exp(-{}_0 g(\vartheta, \varphi)) \quad (4.3)$$

$${}_{1/2} f(\vartheta, \varphi) = 1.3 {}_{1/2} Y_{3/2,1/2}(\vartheta, \varphi) + i {}_{1/2} Y_{3/2,-1/2}(\vartheta, \varphi) \quad (4.4)$$

$${}_{1/2} \tilde{f}(\vartheta, \varphi) = {}_0 \tilde{g}(\vartheta, \varphi) {}_{1/2} f(\vartheta, \varphi) \quad (4.5)$$

$${}_{3/2} h(\vartheta, \varphi) = [{}_{1/2} Y_{11/2,3/2}(\vartheta, \varphi)]^3 \quad (4.6)$$

$${}_{-1/2} k(\vartheta, \varphi) = 0.7 i {}_{-1/2} Y_{5/2,-1/2}(\vartheta, \varphi) + 0.9 {}_{-1/2} Y_{3/2,1/2}(\vartheta, \varphi) \quad (4.7)$$

$${}_{-1/2} \tilde{k}(\vartheta, \varphi) = {}_0 \tilde{g}(\vartheta, \varphi) {}_{-1/2} k(\vartheta, \varphi) \quad (4.8)$$

In Fig. 3 we show  $A_l$  for various combinations that test the various properties outlined. In particular, we observe that functions comprised of a finite number of SWSH are completely captured if  $L$  is greater than the highest harmonic of the linear combination. Products of spin-weighted functions (each individual function comprised of a finite linear combination of SWSH) also are exactly resolved to within numerical error for appropriate  $L$ . Furthermore, we observe the crucial property of exponential convergence for smooth functions.

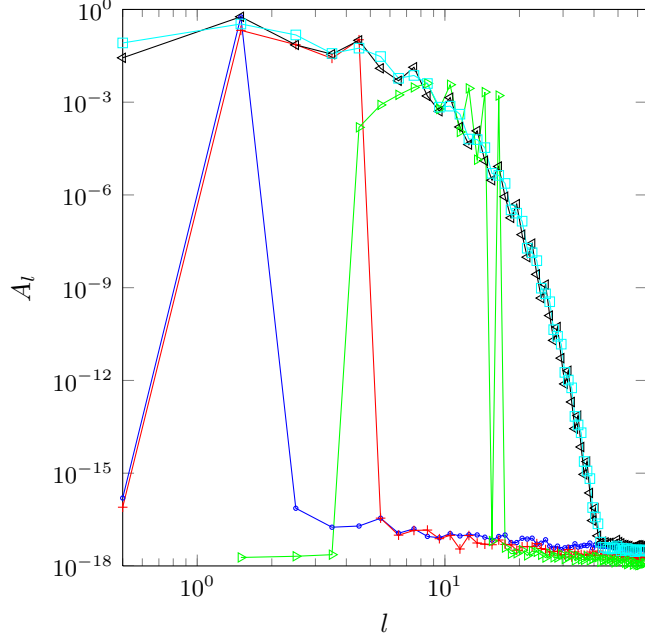


FIGURE 3. (Colour online) The quantity  $A_l$  is depicted and corresponds to: blue "o",  ${}_{1/2}f(\vartheta, \varphi)$ ; red "+",  ${}_{1/2}f(\vartheta, \varphi) {}_0g(\vartheta, \varphi)$ ; black "◁",  ${}_{1/2}\tilde{f}(\vartheta, \varphi)$ ; green "▷",  ${}_{3/2}h(\vartheta, \varphi)$ ; cyan "□",  ${}_{-1/2}\tilde{k}(\vartheta, \varphi)$ . All transforms are performed at a band-limit  $L = 129/2$  and  $s = 1/2, 1/2, 1/2, 3/2, -1/2$  respectively. The functions  ${}_{1/2}f(\vartheta, \varphi)$ ,  ${}_{1/2}f(\vartheta, \varphi) {}_0g(\vartheta, \varphi)$  and  ${}_{3/2}h(\vartheta, \varphi)$  are completely sampled as the average magnitude of coefficients ( $A_l$ ) falls to numerical round-off for  $l$  well below  $L$ . For  ${}_{1/2}\tilde{f}(\vartheta, \varphi)$  and  ${}_{-1/2}\tilde{k}(\vartheta, \varphi)$  we observe the expected exponential decay in  $A_l$ . (See text for details)

## 5. 2 + 1 DIRAC EQUATION

In order to test the SWSH half-integer algorithm we now numerically solve the Dirac equation on a 3-dimensional Lorentz manifold  $(\mathcal{M}, g)$  with topology  $\mathbb{R} \times \mathbb{S}^2$ . Since the Dirac equation on a 3-dimensional manifold is less familiar than its 4-dimensional counterpart we present a detailed derivation in Appendix A and simply state the result here.

We consider the manifold  $\mathcal{M} \sim \mathbb{R} \times \mathbb{S}^2$  with the metric

$$g = dt \otimes dt - \mathcal{F}^{-2}(t, \vartheta, \varphi) (d\vartheta \otimes d\vartheta + \sin^2 \vartheta d\varphi \otimes d\varphi), \quad (5.1)$$

where  $(\vartheta, \varphi)$  are standard polar coordinates for the 2-sphere. The function  $\mathcal{F}(t, \vartheta, \varphi)$  is a conformal factor relating the induced metric at every instant of time  $t$  on  $\mathbb{S}^2$  to the standard metric of the unit 2-sphere.

According to Appendix A the Dirac equation on  $\mathcal{M}$  is given by the following two equations for a spinor  $\psi = [\psi_-, \psi_+]^T$

$$\partial_t \psi_- = -i\mu \psi_- - \frac{1}{2} \partial' \mathcal{F} \psi_+ - \mathcal{F} \partial' \psi_+ + \frac{\mathcal{F}_t}{\mathcal{F}} \psi_-, \quad (5.2)$$

$$\partial_t \psi_+ = i\mu \psi_+ - \frac{1}{2} \bar{\partial} \mathcal{F} \psi_- - \mathcal{F} \bar{\partial} \psi_- + \frac{\mathcal{F}_t}{\mathcal{F}} \psi_+. \quad (5.3)$$

The spinor components  $\psi_{\pm}$  have spin-weight  $\pm \frac{1}{2}$ , while  $\mathcal{F}$  has vanishing spin-weight.

**5.1. Pseudo-spectral method.** While performing a spectral decomposition of variable coefficient PDEs such as Eq. (5.2) and Eq. (5.3) by assuming functions may be expanded as in Eq. (2.2) and then products decomposed as in Eq. (2.12) is possible (see [3] for examples of such expansions in the integer SWSH case) we have found that instead it is far simpler<sup>2</sup> to use a pseudo-spectral (PS) approach.

We outline this as follows: Given the coefficients  ${}_{s_1}\tilde{f}_{l_1m_1}$  and  ${}_{s_2}\tilde{g}_{l_2m_2}$  which represent the functions  ${}_{s_1}f$  and  ${}_{s_2}g$  sampled at a band-limit  $L$  then the coefficients  ${}_{s_1+s_2}\tilde{a}_{lm}$  corresponding to the associated point-wise product  ${}_{s_1}\tilde{f} \cdot {}_{s_2}\tilde{g}$  can be calculated by performing the transformations:

$$\mathcal{F}^{-1} : \left( {}_{s_1}\tilde{f}_{l_1m_1} \right) \mapsto {}_{s_1}\tilde{f}, \quad \mathcal{F}^{-1} : \left( {}_{s_1}\tilde{g}_{l_1m_1} \right) \mapsto {}_{s_2}\tilde{g},$$

subsequently taking the pointwise product and transforming:

$$\mathcal{F} : {}_{s_1}\tilde{f} {}_{s_2}\tilde{g} \mapsto ({}_{s_1+s_2}\tilde{a}_{lm}),$$

we find an approximation to an expansion utilizing Eq. (2.12) directly. We emphasize that this method also easily allows one to take into account the action of the  $\partial, \partial'$  operators on spin-weighted functions by embedding their action as multiplication (see Eq. (2.9) and Eq. (2.10)) in coefficient space, together with taking account of their spin raising and lowering properties when transforms are performed.

We now recast the PDE system of Eq. (5.2) and Eq. (5.3) as an (infinite dimensional) ODE system using the PS method. It is convenient to define the auxiliary fields:

$$\begin{aligned} \Xi_- &:= \mathcal{F}\partial'\psi_+, & \Phi_- &:= \frac{1}{2}\psi_+\partial'\mathcal{F}, & \Psi_- &:= \psi_-\frac{\mathcal{F}_t}{\mathcal{F}}, \\ \Xi_+ &:= \mathcal{F}\partial\psi_-, & \Phi_+ &:= \frac{1}{2}\psi_-\partial\mathcal{F}, & \Psi_+ &:= \psi_+\frac{\mathcal{F}_t}{\mathcal{F}}, \end{aligned} \quad (5.4)$$

where  $\pm$  corresponds to a spin-weight of  $\pm 1/2$ . Using these fields we find that Eq. (5.2) and Eq. (5.3) can be written as:

$$\begin{aligned} \dot{\psi}_{-,lm}(t) &= -i\mu\psi_{-,lm}(t) - \Phi_{-,lm}(t) - \Xi_{-,lm}(t) + \Psi_{-,lm}(t) \\ \dot{\psi}_{+,lm}(t) &= i\mu\psi_{+,lm}(t) - \Phi_{+,lm}(t) - \Xi_{+,lm}(t) + \Psi_{+,lm}(t) \end{aligned} \quad (5.5)$$

We note that in the case of  $\mathcal{F} = 1$ , eqs. (5.2) and (5.3) yield a constant-coefficient PDE system which may be directly decomposed as:

$$\begin{aligned} \dot{\psi}_{-,lm}(t) &= -i\mu\psi_{-,lm}(t) - \left( l + \frac{1}{2} \right) \psi_{+,lm}(t) \\ \dot{\psi}_{+,lm}(t) &= i\mu\psi_{+,lm}(t) + \left( l + \frac{1}{2} \right) \psi_{-,lm}(t) \end{aligned} \quad (5.6)$$

In this case, a solution is readily arrived at:

$$\psi_{\pm,lm}(t) = \frac{1}{\omega_l} \left[ (\omega_l \cos(\omega_l t) \pm i\mu \sin(\omega_l t)) \psi_{\pm,lm}(0) \pm \left( l + \frac{1}{2} \right) \sin(\omega_l t) \psi_{\mp,lm}(0) \right], \quad (5.7)$$

where  $\omega_l := \sqrt{\left( l + \frac{1}{2} \right)^2 + \mu^2}$ .

When  $\mathcal{F} \neq 1$  we numerically construct the spatial representation of the function using Eq. (2.5) with spatial sampling to coincide with the half-integer SWSH transformation. We will also find it useful to introduce the rescaled current component:

$$\tilde{j}^0(t, \vartheta, \varphi) := \frac{1}{\mathcal{F}^2(t, \vartheta, \varphi)} j^0(t, \vartheta, \varphi), \quad (5.8)$$

<sup>2</sup> Indeed the pseudo-spectral method generalises more readily to nonlinear problems.

which with the PS method can be computed using the rescaled fields  $\tilde{\psi}_{\pm} := \psi_{\pm}/\mathcal{F}^2$ . From Eq. (A.11) and Eq. (5.8) the probability  $Q(\Sigma_{\tau})$  can be computed via:

$$Q(\Sigma_{\tau}) = \sum_{l,m} \left( \bar{\psi}_{-,lm} \tilde{\psi}_{+,lm} + \tilde{\psi}_{-,lm} \bar{\psi}_{+,lm} \right). \quad (5.9)$$

**5.2. Numerical solutions and convergence tests.** In this section we examine numerical solutions to the EOM eqs. (5.2) and (5.3) under three conditions: The case  $\mathcal{F} = 1$  (corresponding to a  $\mathbb{S}^2$  spatial geometry), where we numerically solve the system of equations given by the decomposition of Eq. (5.6); the case of a static deformation (time-independent) of  $\mathcal{F}$ ; a time-dependent  $\mathcal{F}$ . In the latter two cases we work with the decomposition of Eq. (5.5). In each case we are free to select arbitrary initial data for  $\psi_{\pm}$ . As convergence tests must be performed for any numerical calculation we begin by briefly summarising the procedure we follow (based on [2]) for doing so, subsequently presenting our results. Aside from presenting convergence for the fields  $\psi_{\pm}$  we also verify that the continuity equation for the current is obeyed and probability is conserved in each case examined.

In using the PS approach of sec. 5.1 to compute the time-evolution of  $\psi_{\pm}$  we solve a truncated ( $l \leq L$ ) ODE system for  $\psi_{\pm,lm}(t)$ . Suppose that we use an explicit, temporal integrator with a fixed time-step  $\delta t$ . The numerically calculated solution for this choice of  $\delta t$  we denote as  $\psi_{\pm,lm}(t; \delta t)$ . Assume that there exists a Taylor expansion of  $\psi_{\pm,lm}(t; \delta t)$  about the exact solution  $\psi_{\pm,lm}(t)$  with error constant terms  $\{E_i\}$ :

$$\psi_{\pm,lm}(t; \delta t) = \psi_{\pm,lm}(t) + \sum_{n=1}^{\infty} \delta t^n E_n. \quad (5.10)$$

Suppose now that the integrator is of order  $p$  so that  $\{E_j\}_{j < p} = 0$ . Thus:

$$\psi_{\pm,lm}(t; \delta t) - \psi_{\pm,lm}(t) = \delta t^p E_p + \mathcal{O}(\delta t^{p+1}). \quad (5.11)$$

By successively rescaling  $\delta t$  with a constant (here 2) and comparing  $\psi_{\pm,lm}(t; \delta t/2^k)$  with  $\psi_{\pm,lm}(t)$  we find:

$$2^{kp} \left\{ \psi_{\pm,lm} \left( t; \frac{1}{2^k} \delta t \right) - \psi_{\pm,lm}(t) \right\} \rightarrow \delta t^p E_p. \quad (5.12)$$

Equation (5.12) may be used in the case when an analytical solution is known. If this is not the case we may instead successively compare  $\psi_{\pm,lm}(t; \delta t/2^k)$  and  $\psi_{\pm,lm}(t; \delta t/2^{k+1})$  which yields:

$$2^{kp} \left\{ \psi_{\pm,lm} \left( t; \frac{1}{2^k} \delta t \right) - \psi_{\pm,lm} \left( t; \frac{1}{2^{k+1}} \delta t \right) \right\} \rightarrow \left( 1 - \frac{1}{2^p} \right) \delta t^p E_p = \delta t^p \tilde{E}_p, \quad (5.13)$$

this is known as a self-consistent convergence test (SCCT) [2]. Note that in both cases (Eq. (5.12) and Eq. (5.13)) we may also make comparisons of functions in the spatial representation by transforming from coefficient-space. In particular, we will consider the maximum, absolute, relative error metric:

$$\epsilon_r(\phi_{\pm}(t, \vartheta, \varphi), \psi_{\pm}(t, \vartheta, \varphi)) := \max_{m,n} \left| 1 - \frac{\phi_{\pm}(t, m\Delta\vartheta, n\Delta\varphi)}{\psi_{\pm}(t, m\Delta\vartheta, n\Delta\varphi)} \right|, \quad (5.14)$$

which allows for the comparison of the two solutions  $\phi_{\pm}$ ,  $\psi_{\pm}$  at sampling nodes  $m\Delta\vartheta$ ,  $n\Delta\varphi$ . We measure error in this manner such that convergence properties of solutions and any potential instability that may result from the SWSH transformation algorithm may be simultaneously inspected.

Having described the methods we use to test convergence of solutions we now examine some example cases. We fix the mass-parameter to be  $\mu = 1.2$  at the outset and choose a temporal range of  $t \in [0, 5]$  throughout. These choices have been

made so as to allow for observation of multiple oscillations of  $\psi_{\pm,lm}(t)$  modes (see Eq. (5.7)) while simultaneously avoiding exact integer multiple of the frequencies  $\omega_l/(2\pi)$ . Note that all specified initial conditions  $\psi_{\pm}|_{t=0}$  are constructed with data as indicated below and then the corresponding coefficients  $\psi_{\pm,lm}|_{t=0}$  rescaled by an overall factor so that  $Q$  is normalized to 1 at  $t = 0$ . For each numerical evolution the temporal integrator we choose is the standard, explicit Runge-Kutta 4th order method (RK4); thus  $p = 4$  in Eq. (5.12) and Eq. (5.13).

For  $\mathcal{F} = 1$  we select the smooth initial data:

$$\psi_{-}(t, \vartheta, \varphi)|_{t=0} = -_{1/2}\tilde{k}(\vartheta, \varphi), \quad \psi_{+}(t, \vartheta, \varphi)|_{t=0} = {}_{1/2}\tilde{f}(\vartheta, \varphi) \quad (5.15)$$

with  $_{-1/2}\tilde{k}(\vartheta, \varphi)$  given by Eq. (4.8) and  ${}_{1/2}\tilde{f}(\vartheta, \varphi)$  given by Eq. (4.5). The system to solve is thus specified by Eq. (5.6) and Eq. (5.15) upon mapping the latter  $\psi_{\pm}(t, \vartheta, \varphi)|_{t=0}$  to coefficient space using the SWSH transformation algorithm. The results of convergence tests (based on Eq. (5.12) with the analytical solution of Eq. (5.7)) of our numerical solution are shown in Fig. 4. We find excellent agreement with the expected 4th order convergence in time for initial data and parameters specified. In particular, we see that the numerical error of the solution is dominated by the temporal discretization. In Fig. 5(a) and Fig. 5(b) we provide representative

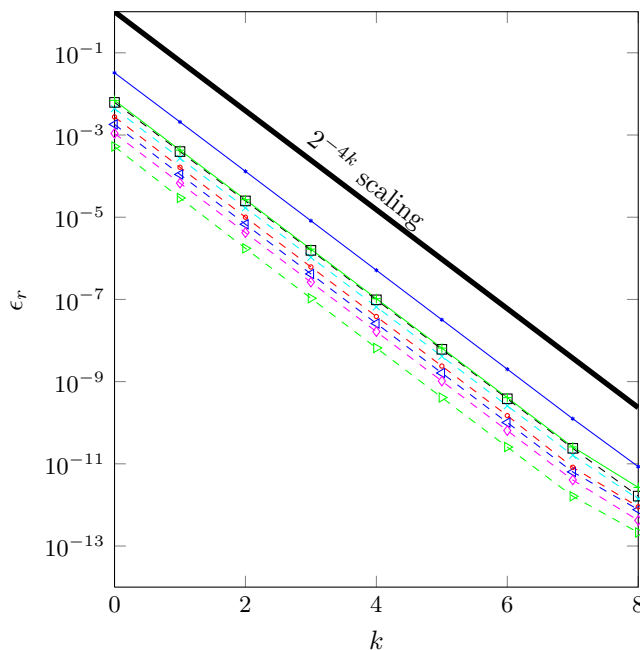


FIGURE 4. (Colour online) Convergence test of numerical solution  $\psi_{\pm}$  (spatial representation) for the case  $\mathcal{F} = 1$ .  $\epsilon_r(\psi_{\pm}) := \epsilon_r(\psi_{\pm}(t; \delta t^k, \vartheta, \varphi), \psi_{\pm}(t, \vartheta, \varphi))$  is displayed at  $t = 5$  for a number of steps  $N = 2^k \times 100$ .  $\psi_{\pm}(t, \vartheta, \varphi)$  is calculated from Eq. (5.7) and the spatial representation found by the SWSH transformation. Blue (dashed), " $\triangleleft$ ":  $L = 17/2$ ,  $\epsilon_r(\psi_{-})$ ; Green (dashed), " $\triangleright$ ":  $L = 17/2$ ,  $\epsilon_r(\psi_{+})$ ; Red (dashed), " $\circ$ ":  $L = 33/2$ ,  $\epsilon_r(\psi_{-})$ ; Cyan (dashed), " $\times$ ":  $L = 33/2$ ,  $\epsilon_r(\psi_{+})$ ; Black (dashed), " $\square$ ":  $L = 65/2$ ,  $\epsilon_r(\psi_{-})$ ; Magenta (dashed), " $\diamond$ ":  $L = 65/2$ ,  $\epsilon_r(\psi_{+})$ ; Blue (solid), " $*$ ":  $L = 129/2$ ,  $\epsilon_r(\psi_{-})$ ; Green (solid), " $+$ ":  $L = 129/2$ ,  $\epsilon_r(\psi_{+})$ . The thick black line corresponds to an expected convergence of 4th order in time. (See text for discussion)

examples of the maximum absolute value of the 3-divergence  $\nabla_\alpha j^\alpha$  (expected to be 0 by Eq. (A.2)) and probability conservation  $|1 - Q|$  (again expected to be 0) at a fixed number of time-steps (temporal discretization). This allows for the examination of the effect of varying the band-limit  $L$  on the evolution of the smooth initial data of Eq. (5.15). In Fig. 5(a) we observe that the numerical error is greatest

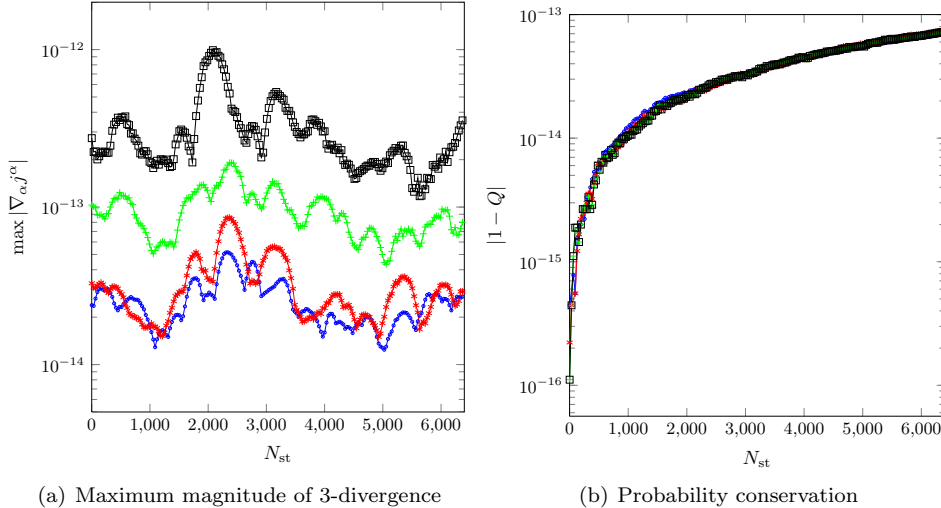


FIGURE 5. (Colour online) Test of the continuity equation and probability conservation for the case  $\mathcal{F} = 1$ . We fix the time-step  $\delta t$  to be  $5/6400$ .  $N_{st}$  indicates the number of time-steps taken from  $t = 0$  (to the maximum  $t = 5$ ). (a) Maximum over all sampled nodes in the spatial representation of  $|\nabla_\alpha j^\alpha|$  (based on Eq. (A.2)) (b) Conservation of probability  $Q$  with time (based on Eq. (5.9)) In both sub-figures: Blue "o":  $L = 17/2$ ; Red "\*":  $L = 33/2$ ; Green "+":  $L = 65/2$ ; Black "□":  $L = 129/2$ . (See text for discussion)

for  $L = 129/2$  and minimizes for  $L = 17/2$  – the reason for this can be explained as follows: From the evolution equation (Eq. (5.6)) we see that coupling does not occur between distinct  $l, m$  modes, only between fixed  $l, m$  of  $\psi_{\pm, lm}$ . Hence we see that if for given  $l, m$  it is the case that  $\psi_{-, lm}|_{t=0} = \psi_{+, lm}|_{t=0} = 0$  then to within numerical tolerance these coefficients should remain 0 over the course of the evolution. Thus for a finite  $L$  we effectively provide a choice of initial data which can be viewed as exact at the specified  $L$ . The error arising from the spectral components of  $\psi_{\pm}$  can hence be entirely attributed to that of the SWSH transformation itself, which scales with increasing  $L$  as shown in Fig. 2. This behaviour can also be observed in Fig. 4 by comparing the numerical error associated with components  $\psi_{\pm}$  at a fixed  $k$  for differing  $L$ . In Fig. 5 we examine the conservation of probability with the quantity  $|1 - Q|$  where  $Q$  is calculated according to Eq. (5.9) and as  $\mathcal{F} = 1$  we may avoid rescaling to  $\tilde{\psi}_{\pm}$  as is required in more general cases. As no SWSH transformations are required to compute this quantity once  $\psi_{\pm, lm}(t)$  is known we find that upon changing  $L$  the previous associated numerical error is not accumulated and the results for  $|1 - Q|$  at differing  $L$  coincide.

For a time independent  $\mathcal{F}$  we select the (finite  $L$ ) initial data  $\psi_{\pm, lm}(t)|_{t=0}$ :

$$\begin{aligned} \psi_{-\frac{1}{2}, -\frac{1}{2}} &= 2, & \psi_{-\frac{1}{2}, \frac{1}{2}} &= \psi_{-\frac{3}{2}, -\frac{3}{2}} = \psi_{-\frac{3}{2}, \frac{3}{2}} = 1, \\ \psi_{-\frac{7}{2}, -\frac{5}{2}} &= i, & \psi_{-\frac{7}{2}, \frac{1}{2}} &= -2i, & \psi_{-\frac{7}{2}, \frac{7}{2}} &= 1, \end{aligned} \quad (5.16)$$

$$\begin{aligned} \psi_{+\frac{1}{2},-\frac{1}{2}} = 3, \quad \psi_{+\frac{1}{2},\frac{1}{2}} = \psi_{+\frac{3}{2},-\frac{3}{2}} = 1, \quad \psi_{+\frac{3}{2},\frac{3}{2}} = 5, \quad \psi_{+\frac{7}{2},-\frac{7}{2}} = 3, \\ \psi_{+\frac{7}{2},-\frac{5}{2}} = 2, \quad \psi_{+\frac{7}{2},-\frac{1}{2}} = 1, \quad \psi_{+\frac{7}{2},\frac{3}{2}} = 2, \quad \psi_{+\frac{7}{2},\frac{5}{2}} = 1, \end{aligned} \quad (5.17)$$

and  $\mathcal{F}$  we choose as:

$$\mathcal{F}_{0,0} = 4, \quad \mathcal{F}_{1,-1} = -\mathcal{F}_{1,1} = \frac{1}{2}, \quad \mathcal{F}_{4,2} = \mathcal{F}_{4,-2} = \frac{1}{10}. \quad (5.18)$$

Together with the above specifications we make use of auxiliary fields as defined in Eq. (5.4) with  $\Psi_{\pm}(t) = 0 \implies \Psi_{\pm,lm}(t) = 0$  and the EOM decomposition of Eq. (5.5). In this case instead of comparing with an analytical solution we perform a self-consistent convergence based on Eq. (5.13). The result of this is presented in Fig. 6. We observe the expected 4th order convergence in time for the numerical

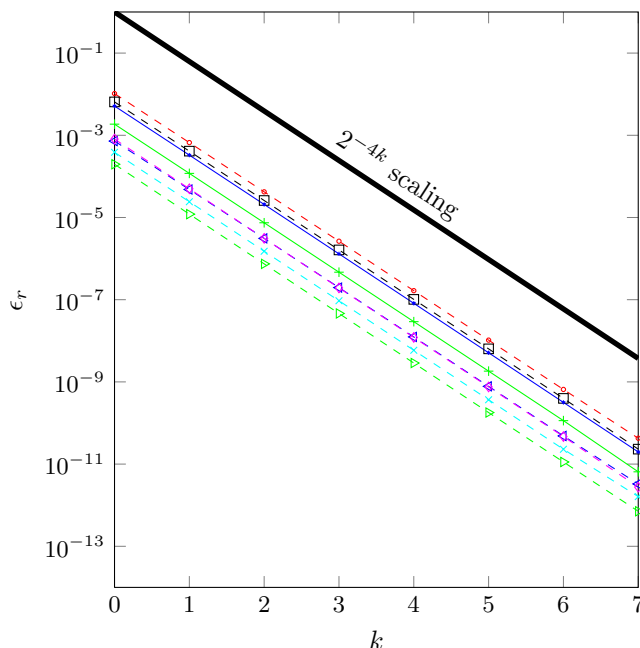


FIGURE 6. (Colour online) SCCT of numerical solution  $\psi_{\pm}$  (spatial representation) for the case of static  $\mathcal{F}$  (Eq. (5.18)).  $\epsilon_r(\psi_{\pm}) := \epsilon_r(\psi_{\pm}(t; \delta t^k, \vartheta, \varphi), \psi_{\pm}(t; \delta t^{k+1}, \vartheta, \varphi))$  is displayed at  $t = 5$  for a number of steps  $N = 2^k \times 100$ . Blue (dashed), " $\triangleleft$ ":  $L = 17/2$ ,  $\epsilon_r(\psi_-)$ ; Green (dashed), " $\triangleright$ ":  $L = 17/2$ ,  $\epsilon_r(\psi_+)$ ; Red (dashed), " $\circ$ ":  $L = 33/2$ ,  $\epsilon_r(\psi_-)$ ; Cyan (dashed), " $\times$ ":  $L = 33/2$ ,  $\epsilon_r(\psi_+)$ ; Black (dashed), " $\square$ ":  $L = 65/2$ ,  $\epsilon_r(\psi_-)$ ; Magenta (dashed), " $\diamond$ ":  $L = 65/2$ ,  $\epsilon_r(\psi_+)$ ; Blue (solid), " $*$ ":  $129/2$ ,  $\epsilon_r(\psi_-)$ ; Green (solid), " $+$ ":  $129/2$ ,  $\epsilon_r(\psi_+)$ . The thick black line corresponds to an expected convergence of 4th order in time. (See text for discussion)

solution  $\psi_{\pm}(t, \vartheta, \varphi)$  at the band limits tested. In Fig. 7(a) and Fig. 7(b) we show representative examples of how the numerical solution obeys the continuity equation and probability conservation respectively<sup>3</sup>. Note that in order to calculate  $Q$  for this case we rescale fields as in Eq. (5.9) and use the full prescription of the PS method (see sec. 5.1). In contrast to the  $\mathcal{F} = 1$  case we now have a variable coefficient EOM and coupling between distinct  $l, m$  modes of  $\psi_{\pm,lm}$  occurs, thus sampling at

<sup>3</sup>The amount of raw data that can be generated at higher  $L$  can grow dramatically - during the calculation we thus only retain the coefficients  $\psi_{\pm,lm}(t)$  at evenly interspersed points on the temporal grid as presented in figures.

a sufficiently high band-limit  $L$  in addition to choosing a sufficiently fine temporal grid is required in order to resolve conservation properties accurately. Finally we

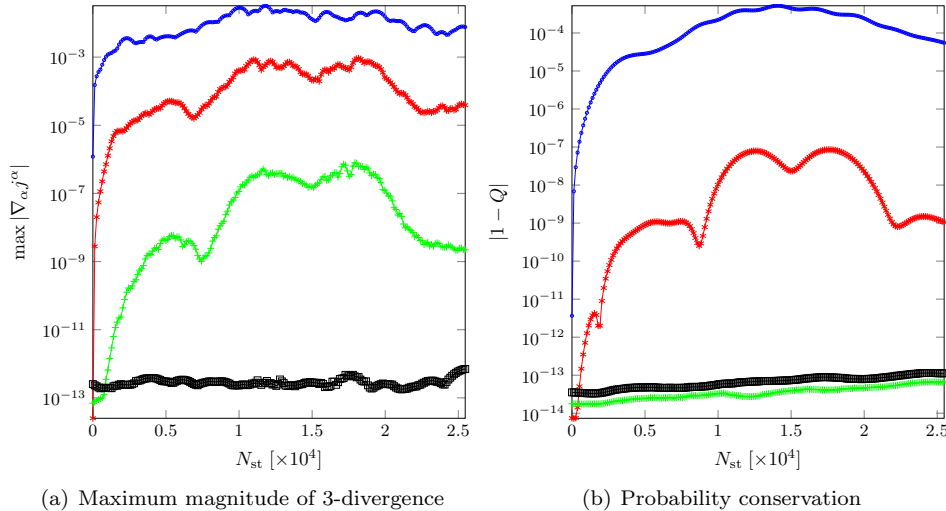


FIGURE 7. (Colour online) Test of the continuity equation and probability conservation for the case of static  $\mathcal{F}$  (Eq. (5.18)). We fix the time-step  $\delta t$  to be  $5/6400$ .  $N_{st}$  indicates the number of time-steps taken from  $t = 0$  (to the maximum  $t = 5$ ). (a) Maximum over all sampled nodes in the spatial representation of  $|\nabla_\alpha j^\alpha|$  (based on Eq. (A.2)) (b) Conservation of probability  $Q$  with time (based on Eq. (5.9)) In both sub-figures: Blue "o":  $L = 17/2$ ; Red "\*":  $L = 33/2$ ; Green "+":  $L = 65/2$ ; Black "□":  $L = 129/2$ . (See text for discussion)

consider a time-dependent  $\mathcal{F}$ . The selection we make is linear interpolation in time between initial  $g(\vartheta, \varphi)$  and final  $h(\vartheta, \varphi)$  static deformations of  $\mathbb{S}^2$ . That is,  $\mathcal{F}(t, \vartheta, \varphi) := (1 - t/t_f)g(\vartheta, \varphi) + (t/t_f)h(\vartheta, \varphi)$  and  $t_f = 5$ . The (real) functions  $g$  and  $h$  we choose to have non-zero  $g_{l,m}$  and  $h_{l,m}$  coefficients:

$$\begin{aligned} g_{0,0} = 8, \quad g_{1,-1} = -g_{1,1} = \frac{5}{2}, \quad g_{4,-2} = g_{4,2} = \frac{1}{10} \\ h_{0,0} = 8, \quad h_{1,-1} = -h_{1,1} = -\frac{5}{2}, \quad h_{4,-2} = h_{4,2} = \frac{1}{10} \end{aligned} \quad (5.19)$$

Initial data  $\psi_{\pm,lm}(t)|_{t=0}$  is selected as in Eq. (5.16) and Eq. (5.17). Together with the above specifications we again make use of auxiliary fields as defined in Eq. (5.4) (note however that  $\Psi_{\pm}(t) \neq 0$ ) and the EOM decomposition of Eq. (5.5). We again perform a self-consistent convergence based on Eq. (5.13). The result of this is presented in Fig. 8. Once again, excellent agreement with the expected 4th order convergence is observed with respect to the temporal scheme. We are again in a situation with a variable coefficient EOM, however now it also becomes non-autonomous. The continuity equation, together with probability conservation must be obeyed in this case also, and indeed we find that provided a sufficiently high band-limit  $L$  is chosen we may resolve these stated properties in our numerical solution (See Fig. 9(a) and Fig. 9(b)).

**5.3. Dirac equation: collapsing background geometry.** Having analysed the numerical properties of our implementation of a pseudo-spectral method for the

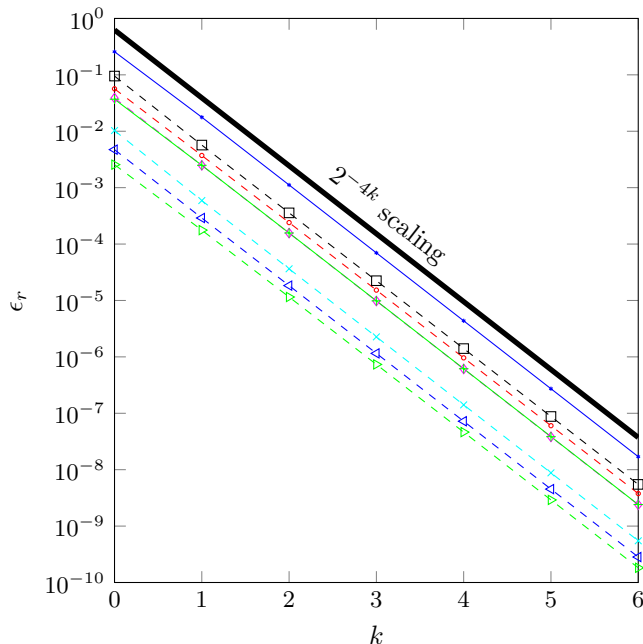


FIGURE 8. (Colour online) SCCT of numerical solution  $\psi_{\pm}$  (spatial representation) for the case of time-dependent  $\mathcal{F}$  (Eq. (5.19)).  $\varepsilon_r(\psi_{\pm}) := \varepsilon_r(\psi_{\pm}(t; \delta t^k, \vartheta, \varphi), \psi_{\pm}(t; \delta t^{k+1}, \vartheta, \varphi))$  is displayed at  $t = 5$  for a number of steps  $N = 2^k \times 200$ . Blue (dashed), " $\triangleleft$ ":  $L = 17/2$ ,  $\varepsilon_r(\psi_-)$ ; Green (dashed), " $\triangleright$ ":  $L = 17/2$ ,  $\varepsilon_r(\psi_+)$ ; Red (dashed), " $\circ$ ":  $L = 33/2$ ,  $\varepsilon_r(\psi_-)$ ; Cyan (dashed), " $\times$ ":  $L = 33/2$ ,  $\varepsilon_r(\psi_+)$ ; Black (dashed), " $\square$ ":  $L = 65/2$ ,  $\varepsilon_r(\psi_-)$ ; Magenta (dashed), " $\diamond$ ":  $L = 65/2$ ,  $\varepsilon_r(\psi_+)$ ; Blue (solid), " $*$ ":  $129/2$ ,  $\varepsilon_r(\psi_-)$ ; Green (solid), " $+$ ":  $129/2$ ,  $\varepsilon_r(\psi_+)$ . The thick black line corresponds to an expected convergence of 4th order in time. (See text for discussion)

Dirac equation we now turn to potential applications. We consider a  $(2 + 1)$  dimensional analogue of the usual Friedmann-Robertson-Walker (FRW) space-time in comoving coordinates. The particular physical scenario we wish to model is an imploding universe with pressure  $P$  and density  $\rho$  equal to zero. We take the scale factor to be  $a(t) = 1 - t = \mathcal{F}(t)^{-1}$ . Thus, we see that at  $t = 0$  the background spatial geometry coincides with that of  $S^2$  upon which initial data for the Dirac equation must be provided.

For many practical purposes it is sufficient to consider an initial Gaussian state when discussing the dynamics of the Dirac equation. For a  $(n-1)$ -sphere embedded in  $\mathbb{R}^n$  the von Mises-Fisher distribution serves as an analogue to the planar Gaussian distribution [18]. The probability density function is given by:

$$f_n(\mathbf{x}; \mathbf{x}_0, \kappa) = \frac{\kappa^{n/2-1}}{(2\pi)^{n/2} I_{n/2-1}(\kappa)} \exp(\kappa \mathbf{x}_0^T \mathbf{x})$$

where  $\kappa \geq 0$ ,  $\|\mathbf{x}_0\| = 1$  and  $I_m(z)$  is the modified Bessel function of the first kind. The parameter  $\kappa$  may be thought of as analogous to the reciprocal of the variance of the Gaussian distribution and  $\mathbf{x}_0$  as the mean direction about which the points  $\mathbf{x}$  cluster. We choose initial data with average momentum 0 where  $j^0|_{t=0} = f_3(\mathbf{x}; \mathbf{x}_0|_{\theta=\pi/3, \phi=\pi/3}, 96)$  and  $j^1 = j^2 = 0$ . For the mass parameter we take  $\mu = 1.2$

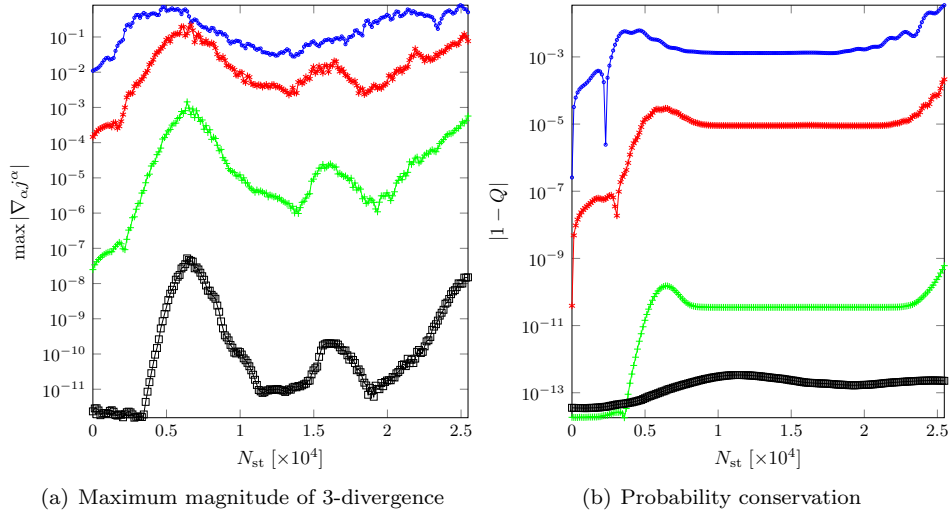


FIGURE 9. (Colour online) Test of the continuity equation and probability conservation for the case of time-dependent  $\mathcal{F}$  (Eq. (5.19)). We fix the time-step  $\delta t$  to be  $5/6400$ .  $N_{st}$  indicates the number of time-steps taken from  $t = 0$  (to the maximum  $t = 5$ ). (a) Maximum over all sampled nodes in the spatial representation of  $|\nabla_\alpha j^\alpha|$  (based on Eq. (A.2)) (b) Conservation of probability  $Q$  with time (based on Eq. (5.9)) In both sub-figures: Blue "o":  $L = 17/2$ ; Red "\*":  $L = 33/2$ ; Green "+":  $L = 65/2$ ; Black "□":  $L = 129/2$ . (See text for discussion)

and evolve Eq.(5.2) and Eq.(5.3) on the temporal range  $t \in [0, 0.99]$ . As before we use explicit RK4 as the temporal integrator and upon performing SCCT (Fig. 10) find 4th order convergence in time as expected. Once again the continuity equation must hold and probability must be conserved. These properties are checked for the present numerical calculation in Fig. 11(a) and Fig. 11(b). For each chosen band-limit we observe growth in numerical error of several orders of magnitude as  $t \rightarrow 0.99$ . This is reasonable when we take into account that the spatial geometry is shrinking to a point ( $a(t) \rightarrow 0$  as  $t \rightarrow 0.99$ ). We now fix the band-limit as  $L = 129/2$  together with temporal grid  $N_{st} = 6.4 \times 10^4$ . For the aforementioned resolutions snapshots of the dynamics are displayed on an Aitoff-Hammer projection [30] in Fig. 12. In Fig. 12(a) we see that the probability density  $j^0$  is initially Gaussian in character and subsequently due to the rotational symmetry of the initial state about the mean direction  $\mathbf{x}_0$  we observe evolution towards a ring-like structure indicating dynamics governed by dispersion (Fig. 12(b)). In Fig. 12(c) we see evolution towards the antipode of  $\mathbf{x}_0$ , however we find that this does not coincide with a reconstruction of the initial condition in the limit  $t \rightarrow 1$  (Fig. 12(d)). Observe that the average amplitude of  $\lim_{t \rightarrow 0} j^0(t)$  increases dramatically; this is to be expected due to conservation of probability  $Q$  and the form of the volume element for this particular geometry used in its calculation (Eq.(A.11)).

## 6. CONCLUSION

We have presented a new spectral algorithm for half-integer spin-weighted functions on  $\mathbb{S}^2$  based on spin-weighted spherical harmonics (SWSH) by extending the method for the integer case presented in [3,15]. Our implementation of this spectral

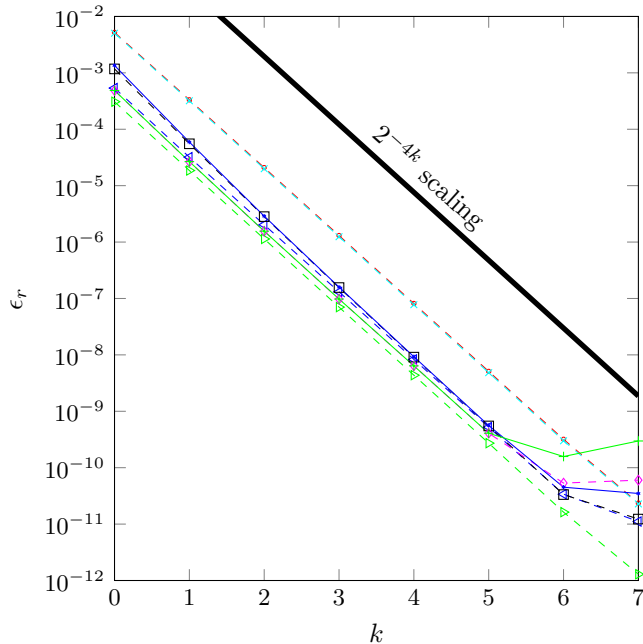


FIGURE 10. (Colour online) SCCT of numerical solution  $\psi_{\pm}$  (spatial representation) for the case of  $\mathcal{F}(t)^{-1} = a(t) = 1 - t$ .  $\varepsilon_r(\psi_{\pm}) := \varepsilon_r(\psi_{\pm}(t; \delta t^k, \vartheta, \varphi), \psi_{\pm}(t; \delta t^{k+1}, \vartheta, \varphi))$  is displayed at  $t = 0.99$  for a number of steps  $N = 2^k \times 4000$ . Blue (dashed), " $\triangleleft$ ":  $L = 17/2$ ,  $\varepsilon_r(\psi_-)$ ; Green (dashed), " $\triangleright$ ":  $L = 17/2$ ,  $\varepsilon_r(\psi_+)$ ; Red (dashed), " $\circ$ ":  $L = 33/2$ ,  $\varepsilon_r(\psi_-)$ ; Cyan (dashed), " $\times$ ":  $L = 33/2$ ,  $\varepsilon_r(\psi_+)$ ; Black (dashed), " $\square$ ":  $L = 65/2$ ,  $\varepsilon_r(\psi_-)$ ; Magenta (dashed), " $\diamond$ ":  $L = 65/2$ ,  $\varepsilon_r(\psi_+)$ ; Blue (solid), " $*$ ":  $129/2$ ,  $\varepsilon_r(\psi_-)$ ; Green (solid), " $+$ ":  $129/2$ ,  $\varepsilon_r(\psi_+)$ . The thick black line corresponds to an expected convergence of 4th order in time. (See text for discussion)

algorithm shows excellent agreement with the theory we have presented. Indeed we find that the numerical error scaling comparable to the integer SWSH algorithm [15] and that exponential convergence properties are displayed as anticipated. Furthermore, the expected algorithmic complexity of  $\mathcal{O}(L^3)$  is retained. In addition, we have outlined how one may construct the  $2+1$  Dirac equation on a curved space-time, adapting the result to the  $\mathfrak{d}$ -formalism and for a geometry with spatial topology of  $\mathbb{S}^2$ . Viewing the Dirac equation as an IVP we demonstrated how a pseudo-spectral approach can be combined with the half-integer SWSH algorithm and analysed several different situations with distinct spatial geometries, examples including linear interpolation between distinct spatial configurations with time and the case of an imploding  $2+1$  FRW-like model. The numerical solutions that we constructed obey anticipated convergence rates for the temporal solver used (explicit RK4) and physical invariants (current continuity and probability) are shown to be preserved during the time-evolution to an excellent degree.

## 7. ACKNOWLEDGMENT

JF is grateful to G. Sparling for several enlightening discussions. This research was partly supported by the Marsden Fund of the Royal Society of New Zealand.

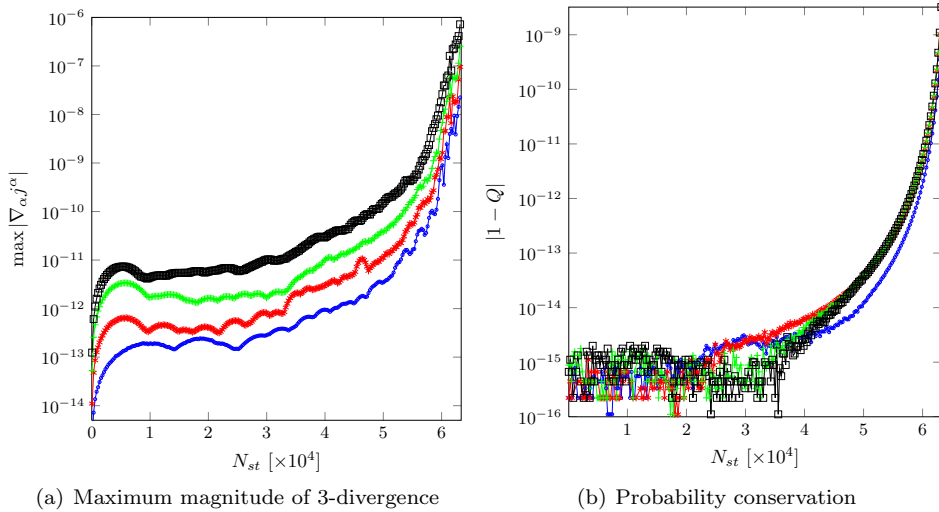


FIGURE 11. (Colour online) Test of the continuity equation and probability conservation for the case of  $\mathcal{F}(t)^{-1} = a(t) = 1 - t$ . We fix the time-step  $\delta t$  to be  $0.99/6.4 \times 10^4$ .  $N_{st}$  indicates the number of time-steps taken from  $t = 0$  (to the maximum  $t = 0.99$ ). (a) Maximum over all sampled nodes in the spatial representation of  $|\nabla_{\alpha} j^{\alpha}|$ . (b) Conservation of probability  $Q$  with time. In both subfigures: Blue "o":  $L = 17/2$ ; Red "\*":  $L = 33/2$ ; Green "+":  $L = 65/2$ ; Black "□":  $L = 129/2$ . (See text for discussion)

#### APPENDIX A. THE DIRAC EQUATION ON A 3-DIMENSIONAL LORENTZ MANIFOLD

Let  $\mathbb{V}$  be a  $n$ -dimensional real vector space equipped with a quadratic form  $\eta$  with signature  $n-2$ , i.e.,  $\eta$  can be represented in diagonal form as  $\eta = \text{diag}(1, -1, \dots, -1)$ . Let  $\mathfrak{c}(\mathbb{V}, \eta)$  be the Clifford algebra associated to  $(\mathbb{V}, \eta)$ . This is the unique algebra with unit  $\mathbf{1}$  and so called structure map  $\gamma : \mathbb{V} \rightarrow \mathfrak{c}(\mathbb{V}, \eta)$  such that for every  $v \in \mathbb{V}$  the relation  $\gamma(v)\gamma(v) = \eta(v, v)\mathbf{1}$  holds. Let  $(e_1, \dots, e_n)$  be a basis of  $\mathbb{V}$  and define  $\eta_{ab} = \eta(e_a, e_b)$  and  $\gamma_a = \gamma(e_a)$ . Then, by polarization of the defining relation, one finds the well-known Clifford-Dirac anti-commutator relations

$$\{\gamma_a, \gamma_b\} = \gamma_a \gamma_b + \gamma_b \gamma_a = 2\eta_{ab}\mathbf{1}.$$

Irreducible representations  $S$  of the Clifford algebras have dimensions  $N = 2^{n/2}$  for  $n$  even and  $N = 2^{(n-1)/2}$  for  $n$  odd. It is well known (see [26]) that these representations can be constructed recursively from the lower dimensional ones. The representation space  $S$  of the Clifford algebra  $\mathfrak{c}(\mathbb{V}, \eta)$  is called the spin space. Depending on the particular case, the spin space is equipped with certain invariant structures, see [26], [27], [31] for detailed discussions.

The commutators of the generators  $\gamma_{ab} := \gamma_{[a}\gamma_{b]} = \frac{1}{2}[\gamma_a, \gamma_b]$  generate a Lie algebra with commutation relations

$$[\gamma_{ab}, \gamma_{cd}] = \eta_{cb}\gamma_{ad} - \eta_{ca}\gamma_{bd} - \eta_{db}\gamma_{ac} + \eta_{da}\gamma_{bc}.$$

These are the commutation relations for the Lie algebra  $\mathfrak{o}(\eta)$  of the (pseudo-) orthogonal group  $O(\eta)$  associated with the bilinear form  $\eta$ . This Lie algebra acts on the subspace  $\gamma[\mathbb{V}] \subset \mathfrak{c}(\mathbb{V}, \eta)$  as follows: for any skew bi-vector  $w^{ab}$  and every vector  $v^a$  we define  $\gamma(w) := w^{ab}\gamma_{ab}$  and  $\gamma(v) = v^a\gamma_a$ , then the action of  $\mathfrak{o}(\eta)$  is via

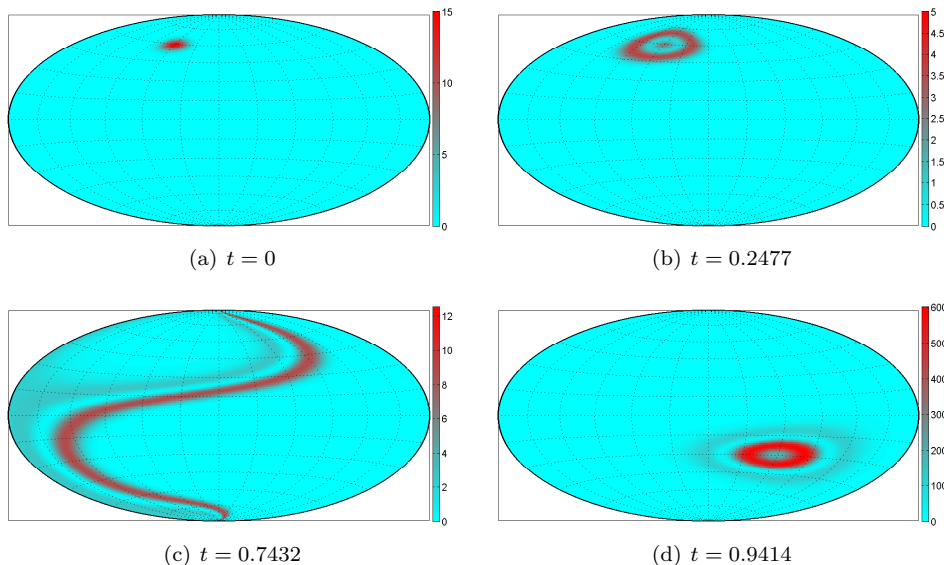


FIGURE 12. (Colour online) Aitoff-Hammer projection of the probability density  $j^0$  associated with the (2+1) dimensional Dirac equation on FRW background. Note that during the course of the time evolution the spatial radius  $a(t)$  of the spherical projection in each sub-figure is distinct, furthermore the colour scaling also varies. See text for discussion.

commutation in  $\mathfrak{c}(\mathbb{V}, \eta)$

$$\mathfrak{o}(\eta) \times \gamma[\mathbb{V}] \rightarrow \gamma[\mathbb{V}], \quad (\gamma(w), \gamma(v)) \mapsto \gamma(w)\gamma(v) - \gamma(v)\gamma(w).$$

We can see the corresponding action on  $\mathbb{V}$  from the explicit calculation

$$\gamma(w)\gamma(v) - \gamma(v)\gamma(w) = w^{ab}v^c (\gamma_{ab}\gamma_c - \gamma_c\gamma_{ab}) = w^{ab}v^c (\eta_{bc}\gamma_a - \eta_{ac}\gamma_b) = 2w^a{}_b v^b \gamma_a.$$

Thus, the action on  $\gamma[\mathbb{V}]$  corresponds to the linear mapping defined by  $2w^a{}_b$  on  $\mathbb{V}$ , which is clearly anti-symmetric with respect to  $\eta$ . The same Lie algebra also acts on the spin-space  $S$  via the representation of the Clifford algebra

$$\mathfrak{o}(\eta) \times S \rightarrow S, \quad (\gamma(w), \psi) \mapsto \gamma(w)\psi.$$

In order to make use of spinors on the manifold  $\mathcal{M}$  we associate at every point  $x \in \mathcal{M}$  the Clifford algebra  $\mathfrak{c}(T_x\mathcal{M}, g_x)$  and its representation space which we denote by  $S_x$ . The rigorous construction is invariantly described in terms of (associated) vector bundles but we will not go into the details here. Instead we refer to [17] for a complete description<sup>4</sup>. The collection of all spin spaces  $S_x$  forms the spin bundle  $S(\mathcal{M})$  over  $\mathcal{M}$  and sections of this bundle are referred to as spinor fields or simply spinors. Similarly, we obtain the Clifford bundle as the collection of all Clifford algebras  $\mathfrak{c}(T_x\mathcal{M}, g_x)$ . The structure maps defined at every point  $x$  yield a bundle map  $\gamma$  from the tangent bundle  $T\mathcal{M}$  to the Clifford bundle, assigning to every tangent vector  $v \in T_x\mathcal{M}$  an element  $\gamma_x(v)$  in the Clifford algebra at  $x$ .

The connection  $\nabla$  on  $\mathcal{M}$  can be lifted to a connection also denoted by  $\nabla$  on  $S(\mathcal{M})$  (see [37]). It can be uniquely characterized by the fact that the structure map  $\gamma$  and the invariant structures on the spin spaces are covariantly constant. With this

<sup>4</sup>Note, that in the general case there are global topological obstructions to the existence of these bundles, see [17, 26]. However, since we are interested mainly in the 3-dimensional case where these obstructions do not exist we will not discuss them here.

connection one can define the Dirac operator on  $\mathcal{M}$  as follows: we pick a basis  $(e_1, \dots, e_n)$  of the tangent space  $T_x\mathcal{M}$  at each  $x \in \mathcal{M}$ . Now the anti-commutator relations are

$$\{\gamma_a, \gamma_b\} = 2g_{ab}\mathbf{1}$$

which hold at every  $x \in \mathcal{M}$  with the appropriate definition of  $g_{ab}$  and  $\gamma_a$ . The Dirac operator  $\mathcal{D}$  acting on spinor fields  $\psi$  is defined by

$$\mathcal{D}\psi := g^{ab}\gamma(e_a)\nabla_{e_b}\psi = \gamma^a\nabla_{e_a}\psi. \quad (\text{A.1})$$

In this paper we assume the vector space  $\mathbb{V}$  to have dimension 3 and to be equipped with a metric  $\eta$  with signature  $(+, -, -)$ . The corresponding Clifford algebra  $\mathfrak{c}(\mathbb{V}, \eta)$  has a 4-dimensional real representation [27, 31], which may conveniently be described within  $M(2, \mathbb{C})$  as the real algebra generated by the ‘Dirac matrices’

$$\gamma_0 = \begin{bmatrix} -1 & 0 \\ 0 & 1 \end{bmatrix}, \quad \gamma_1 = \begin{bmatrix} 0 & 1 \\ -1 & 0 \end{bmatrix}, \quad \gamma_2 = \begin{bmatrix} 0 & i \\ i & 0 \end{bmatrix}.$$

The spin space is  $\mathbb{C}^2$  (regarded as a 4-dimensional real vector space) and carries a sesquilinear form (Hermitian inner product) defined by

$$\langle \psi, \phi \rangle := \psi^* \gamma_0 \phi,$$

where  $\psi^*$  is the Hermitian conjugate of  $\psi$ . For given spinors  $\psi = \begin{bmatrix} \psi_1 \\ \psi_2 \end{bmatrix}$  and  $\phi = \begin{bmatrix} \phi_1 \\ \phi_2 \end{bmatrix}$  this product is

$$\langle \psi, \phi \rangle = -\bar{\psi}_1\phi_1 + \bar{\psi}_2\phi_2.$$

The generators are symmetric with respect to this product, i.e., we have

$$\langle \psi, \gamma_a \phi \rangle = \langle \gamma_a \psi, \phi \rangle.$$

Given two spinors  $\phi$  and  $\psi$  there is a naturally defined covector  $\alpha = \alpha(\phi, \psi)$  with components  $\alpha_a = \langle \phi, \gamma_a \psi \rangle$ . When  $\phi = \psi$ , then this covector is

$$\alpha = [|\psi_1|^2 + |\psi_2|^2, -\bar{\psi}_1\psi_2 - \bar{\psi}_2\psi_1, i(\bar{\psi}_2\psi_1 - \bar{\psi}_1\psi_2)].$$

Hence, it is real and null whenever  $\langle \psi, \psi \rangle = 0$ .

The commutators of the Dirac matrices  $\gamma_a$  are infinitesimal generators of the spin group  $\text{Spin}(1, 2)$ . They can be written here in form

$$\gamma_a \gamma_b - \gamma_b \gamma_a = 2i\epsilon_{ab}{}^c \gamma_c.$$

Choosing an orthonormal frame  $(e_0, e_1, e_2)$  on  $\mathcal{M}$  we can express the Dirac operator on  $\mathcal{M}$  with respect to the chosen frame explicitly. To this end we need the Ricci rotation coefficients for the frame defined by

$$\nabla_{e_a} e_b = \Gamma_{ab}{}^c e_c.$$

The condition that the structure map be covariantly constant translates into the equation

$$\Gamma_{ab}{}^c \gamma_c = \Upsilon_b \gamma_a - \gamma_a \Upsilon_b$$

where the  $\Upsilon_b$ , which depend on the point  $x \in \mathcal{M}$ , are endomorphisms of the spin space  $S_x$ . More precisely, they are linear combinations of the infinitesimal generators of  $\text{Spin}(1, 2)$ . This equation can be solved uniquely for the  $\Upsilon$  and yields

$$\Upsilon_a = -\frac{i}{2}\Gamma_{ba}{}^c \epsilon_c{}^{bd} \gamma_d.$$

The connection defined in this way also leaves the complex structure and the sesquilinear product invariant. With these ‘spin coefficient’ matrices we can express the Dirac operator acting on an arbitrary spinor  $\psi$  as

$$\mathcal{D}\psi = \eta^{ab}\gamma_a (e_b(\psi) + \Upsilon_b \psi).$$

The Dirac equation on  $\mathcal{M}$  can be obtained from a variational principle. For any given spinor field  $\psi$  with compact support on  $\mathcal{M}$  we can write down the action functional

$$\mathfrak{A}[\psi] := \int_{\mathcal{M}} i \langle \psi, \mathcal{D}\psi \rangle + \mu \langle \psi, \psi \rangle d\mathcal{M},$$

where here and later on  $d\mathcal{M}$  denotes the invariant volume form on a manifold  $\mathcal{M}$ . This defines a real number since the imaginary part can be rewritten as

$$i \int_{\mathcal{M}} \langle \psi, \mathcal{D}\psi \rangle + \langle \psi, \mathcal{D}\psi \rangle d\mathcal{M} = i \int_{\mathcal{M}} \nabla_a \alpha^a d\mathcal{M} = 0.$$

Variation with respect to  $\psi$  yields the Dirac equation

$$i\mathcal{D}\psi + \mu\psi = 0.$$

To every solution  $\psi$  of the Dirac equation the covector  $\alpha_a$  defines a conserved current  $j^a$  denoted by

$$j^a = \langle \psi, \gamma^a \psi \rangle.$$

Taking the divergence of this equation we find

$$\begin{aligned} \nabla_a j^a &= \langle \nabla_a \psi, \gamma^a \psi \rangle + \langle \psi, \gamma^a \nabla_a \psi \rangle \\ &= \langle \mathcal{D}\psi, \psi \rangle + \langle \psi, \mathcal{D}\psi \rangle = \langle i\mu\psi, \psi \rangle + \langle \psi, i\mu\psi \rangle = 0. \end{aligned} \quad (\text{A.2})$$

With this current we can define a conserved quantity in the usual way. Let  $t$  be a time coordinate for  $\mathcal{M}$  defined on an interval  $I = [0, T]$  for some arbitrary  $T$  and let  $\Sigma$  be a 2-dimensional manifold. We assume that  $I \times \Sigma$  is embedded into  $\mathcal{M}$  as a 3-dimensional submanifold  $\mathcal{V}$  via the embedding  $i : I \times \Sigma \hookrightarrow \mathcal{M}$ . Then  $i_t : \Sigma \rightarrow \mathcal{M}, x \mapsto (t, x)$  embeds  $\Sigma$  as a space-like hyper-surface  $\Sigma_t$  into  $\mathcal{M}$ . Let  $\mathcal{S} = \partial\Sigma$  be the boundary of  $\Sigma$ , which  $i_t$  embeds as a 1-dimensional submanifold  $\mathcal{S}_t$  into  $\mathcal{M}$ . Now the boundary of  $\mathcal{V}$  is  $\mathcal{V} = \Sigma_0 \cup \mathcal{T} \cup \Sigma_T$  where  $\mathcal{T} = \bigcup_{t \in I} \mathcal{S}_t$ .

Integrating the divergence equation over  $\mathcal{V}$  and using the generalised Stokes' theorem we obtain

$$0 = \int_{\mathcal{V}} \nabla_a j^a d\mathcal{V} = \int_{\partial\mathcal{V}} j^a d\mathcal{V}_a,$$

where we denote the hyper-surface forms on the boundary  $\partial\mathcal{V}$  by  $d\mathcal{V}_a$ . Introducing the future-pointing time-like normal  $t_a$  to the hyper-surfaces  $\Sigma_t$  and the outward normal  $n_a$  to  $\mathcal{T}$  we can write

$$\int_{\Sigma_0} j^a t_a d\Sigma = \int_{\Sigma_T} j^a t_a d\Sigma + \int_{\mathcal{T}} j^a n_a d\mathcal{T}.$$

Defining the scalar ‘‘charge’’ (also interpreted as probability)  $Q$  and its flux  $J$  by

$$Q(t) = \int_{\Sigma_t} j^a t_a d\Sigma, \quad J(t) = \int_{\mathcal{S}_t} j^a n_a d\mathcal{S} \quad (\text{A.3})$$

we can write the balance law

$$Q(T) = Q(0) + \int_0^T J(t) dt \quad (\text{A.4})$$

which holds for arbitrary values of  $T$ . With appropriate boundary conditions (for instance, when  $\Sigma$  has no boundary as we assume below) for the Dirac field one can make the flux vanish so that the balance law turns into the conservation equation for  $Q$

$$Q(T) = Q(0).$$

We now specialize to the case  $\mathcal{M} \sim \mathbb{R} \times \mathbb{S}^2$  with the metric

$$g = dt \otimes dt - \mathcal{F}^{-2}(t, \vartheta, \varphi) (d\vartheta \otimes d\vartheta + \sin^2 \vartheta d\varphi \otimes d\varphi), \quad (\text{A.5})$$

where  $(\vartheta, \varphi)$  are standard polar coordinates for the 2-sphere. The function  $\mathcal{F}(t, \vartheta, \varphi)$  is a conformal factor relating the induced metric at every instant of time  $t$  on  $\mathbb{S}^2$  to the standard metric of the unit 2-sphere. We choose the orthonormal frame as

$$e_0 = \partial_t, \quad e_1 = \mathcal{F} \partial_\vartheta, \quad e_2 = \mathcal{F} \csc \vartheta \partial_\varphi. \quad (\text{A.6})$$

The non-vanishing Ricci rotation coefficients are

$$\Gamma_{11}^0 = -\frac{\mathcal{F}_t}{\mathcal{F}}, \quad \Gamma_{22}^0 = -\frac{\mathcal{F}_t}{\mathcal{F}}, \quad \Gamma_{12}^1 = -\frac{\mathcal{F}_\varphi}{\sin \vartheta}, \quad \Gamma_{22}^1 = -(\mathcal{F}_\vartheta - \mathcal{F} \cot \vartheta). \quad (\text{A.7})$$

From these we obtain the non-vanishing ‘spin coefficient’ matrices

$$\Upsilon_1 = \frac{i}{2} \begin{bmatrix} \mathcal{F}_\varphi / \sin \vartheta & i\mathcal{F}_t / \mathcal{F} \\ i\mathcal{F}_t / \mathcal{F} & -\mathcal{F}_\varphi / \sin \vartheta \end{bmatrix}, \quad \Upsilon_2 = \frac{i}{2} \begin{bmatrix} \mathcal{F}_\vartheta - \mathcal{F} \cot \vartheta & -\mathcal{F}_t / \mathcal{F} \\ \mathcal{F}_t / \mathcal{F} & -\mathcal{F}_\vartheta + \mathcal{F} \cot \vartheta \end{bmatrix}. \quad (\text{A.8})$$

In order to make use of the spin-weighted formalism we need to identify the spin-weights of the quantities involved. To this end we consider the infinitesimal rotations of tangent vectors to the sphere as induced by the  $(1, 2)$ -Lorentz group  $O(\eta)$  at every point on  $\mathcal{M}$ . Consider the infinitesimal rotation given by  $\frac{1}{2}\gamma_{12} = \frac{i}{2}\gamma_0$  acting as follows on the two frame vectors on the sphere

$$\gamma(e_1) = \gamma_1 \mapsto \frac{1}{2} [\gamma_{12}, \gamma_1] = \gamma_2, \quad \gamma(e_2) = \gamma_2 \mapsto \frac{1}{2} [\gamma_{12}, \gamma_2] = -\gamma_1.$$

In terms of the complex null-vector  $m = \frac{1}{\sqrt{2}}(e_1 - ie_2)$  this is

$$\gamma(m) \mapsto i\gamma(m),$$

so  $\frac{1}{2}\gamma_{12}$  generates the frame rotations  $m \mapsto e^{i\alpha} m$ . But it also acts on the spin-space at each point: for every spinor  $\psi = [\psi_1, \psi_2]^T$  we have

$$\frac{1}{2}\gamma_{12}\psi = \frac{i}{2}\gamma_0 \begin{bmatrix} \psi_1 \\ \psi_2 \end{bmatrix} = \frac{i}{2} \begin{bmatrix} -\psi_1 \\ \psi_2 \end{bmatrix}.$$

Therefore, assigning spin-weight  $+1$  to  $m$  results in the spin-weights  $-\frac{1}{2}$  and  $+\frac{1}{2}$  for  $\psi_1$  and  $\psi_2$ , respectively. Henceforth, we denote the spinor  $\psi$  therefore by  $\psi = [\psi_-, \psi_+]^T$ . Since  $\mathcal{F}$  is a scalar function it has spin-weight 0.

Now we are in a position to write down the Dirac equation. Using (A.1), (A.6), (A.7) and (A.8) we find the two equations

$$\partial_t \psi_- = -i\mu \psi_- - \frac{1}{2} \bar{\partial}' \mathcal{F} \psi_+ - \mathcal{F} \bar{\partial}' \psi_+ + \frac{\mathcal{F}_t}{\mathcal{F}} \psi_-, \quad (\text{A.9})$$

$$\partial_t \psi_+ = i\mu \psi_+ - \frac{1}{2} \bar{\partial} \mathcal{F} \psi_- - \mathcal{F} \bar{\partial} \psi_- + \frac{\mathcal{F}_t}{\mathcal{F}} \psi_+. \quad (\text{A.10})$$

The probability or charge density is

$$j^0 = |\psi_+|^2 + |\psi_-|^2.$$

We take  $\mathcal{V}$  in the form  $(0, t) \times \mathbb{S}^2$  with hyper-surfaces of constant time  $\Sigma_\tau \sim \mathbb{S}^2$  then the ‘charge’ integral as defined in (A.3) yields the expression

$$Q(\tau) = \int_{\mathbb{S}^2} |\psi_+(\tau, \vartheta, \varphi)|^2 + |\psi_-(\tau, \vartheta, \varphi)|^2 \frac{\sin \vartheta \, d\vartheta \, d\varphi}{\mathcal{F}^2(\tau, \vartheta, \varphi)}.$$

Since  $\Sigma_\tau \sim \mathbb{S}^2$  has no boundary, (A.4) implies that for every  $\tau \in (0, T)$

$$Q(\tau) = Q(0) = \text{const.} \quad (\text{A.11})$$

## REFERENCES

- [1] ASHCROFT, N. W., AND MERMIN, N. D. *Solid State Physics*. Saunders College, 1976.
- [2] BAUMGARTE, T., AND SHAPIRO, S. *Numerical Relativity: Solving Einstein's Equations on the Computer*. Cambridge University Press, 2010.
- [3] BEYER, F., DASZUTA, B., FRAUENDIENER, J., AND WHALE, B. Numerical evolutions of fields on the 2-sphere using a spectral method based on spin-weighted spherical harmonics. *Classical and Quantum Gravity* 31, 7 (2014), 075019.
- [4] BOYD, J. P. *Chebyshev and Fourier spectral methods*, 2 ed. Dover Publications, Inc. New York, 2001.
- [5] CASTRO NETO, A. H., GUINEA, F., PERES, N. M. R., NOVOSELOV, K. S., AND GEIM, A. K. The electronic properties of graphene. *Rev. Mod. Phys.* 81 (Jan 2009), 109–162.
- [6] DRAY, T. A unified treatment of Wigner D-functions, spin-weighted spherical harmonics, and monopole harmonics. *Journal of Mathematical Physics* 27, 3 (1986), 781–792.
- [7] FILLION-GOURDEAU, F., LORIN, E., AND BANDRAUK, A. D. Numerical solution of the time-dependent Dirac equation in coordinate space without fermion-doubling. *Computer Physics Communications* 183, 7 (2012), 1403 – 1415.
- [8] FILLION-GOURDEAU, F., LORIN, E., AND BANDRAUK, A. D. A split-step numerical method for the time-dependent Dirac equation in 3-D axisymmetric geometry. *Journal of Computational Physics* 272, 0 (2014), 559 – 587.
- [9] GOLDBERG, J. N., MACFARLANE, A. J., NEWMAN, E. T., ROHRLICH, F., AND SUDARSHAN, E. C. G. Spin- $s$  spherical harmonics and  $\bar{o}$ . *J. Math. Phys.* 8 (1967), 2155.
- [10] FINSTER, F., KAMRAN, N., SMOLLER, J., AND YAU, S.-T. Decay of solutions of the wave equation in the Kerr geometry. *Comm. Math. Phys.*, 264(2) (2006), 465503.
- [11] GRANDCLÉMENT, P., AND NOVAK, J. Spectral methods for numerical relativity. *Living Rev. Relativity* 12, 1 (2009).
- [12] HAMMER, R., AND PÖTZ, W. Staggered grid leap-frog scheme for the Dirac equation. *Computer Physics Communications* 185, 1 (2014), 40 – 52.
- [13] HAMMER, R., PÖTZ, W., AND ARNOLD, A. Single-cone real-space finite difference scheme for the time-dependent Dirac equation. *Journal of Computational Physics* 265, 0 (2014), 50 – 70.
- [14] HESTHAVEN, J., GOTTLIEB, S., AND GOTTLIEB, D. *Spectral Methods for Time-Dependent Problems*. Cambridge Monographs on Applied and Computational Mathematics. Cambridge University Press, 2007.
- [15] HUFFENBERGER, K. M., AND WANDEL, B. D. Fast and exact spin- $s$  spherical harmonic transforms. *Astro. J. Suppl. Series* 189 (2010), 255–260.
- [16] KATZNELSON, Y. *An Introduction to Harmonic Analysis*, 3 ed. Cambridge University Press, 2004.
- [17] LAWSON, H. B., AND MICHELSON, M.-L. *Spin geometry*. Princeton University Press, 1990.
- [18] MARDIA, K., AND JUPP, P. *Directional Statistics*. Wiley Series in Probability and Statistics. Wiley, 2009.
- [19] MCEWEN, J. D., AND WIAUX, Y. A novel sampling theorem on the sphere. *Signal Processing, IEEE Transactions on* 59 (2011), 5876–5887.
- [20] MOCKEN, G. R., AND KEITEL, C. H. Quantum dynamics of relativistic electrons. *Journal of Computational Physics* 199, 2 (2004), 558 – 588.
- [21] MOCKEN, G. R., AND KEITEL, C. H. FFT-split-operator code for solving the Dirac equation in 2+1 dimensions. *Computer Physics Communications* 178, 11 (2008), 868 – 882.
- [22] MOMBARGER, K., BELKACEM, A., AND SRENSSEN, A. H. Numerical treatment of the time-dependent Dirac equation in momentum space for atomic processes in relativistic heavy-ion collisions. *Phys. Rev. A* 53 (Mar 1996), 1605–1622.
- [23] NEWMAN, E. T., AND PENROSE, R. Note on the Bondi-Metzner-Sachs group. *Journal of Mathematical Physics* 7 (1966), 863–870.
- [24] NIELSEN, H., AND NINOMIYA, M. A no-go theorem for regularizing chiral fermions. *Physics Letters B* 105, 2-3 (1981), 219 – 223.
- [25] PENROSE, R., AND RINDLER, W. *Two-Spinor Calculus and Relativistic Fields*, vol. 1 of *Spinors and Space-Time*. Cambridge University Press, 1984.
- [26] PENROSE, R., AND RINDLER, W. *Two-Spinor Calculus and Relativistic Fields*, vol. 2 of *Spinors and Space-Time*. Cambridge University Press, 1986.
- [27] PORTEOUS, I. *Clifford algebras and the classical groups*. Cambridge University Press, Cambridge, 1995.
- [28] RISBO, T. Fourier transform summation of Legendre series and D-functions. *J. Geodesy* 70 (1996), 383–396.

- [29] SAKURAI, J., AND TUAN, S. *Modern Quantum Mechanics*. Addison-Wesley Reading (Mass.), 1994.
- [30] SNYDER, J. P. *Map Projections: A Working Manual*. USGS Numbered Series 1395, Geological Survey (U.S.), 1987.
- [31] SPARLING, G. A. J. The magic of twistor theory. University of Pittsburgh preprint, unpublished.
- [32] STACEY, R. Eliminating lattice fermion doubling. *Phys. Rev. D* *26* (Jul 1982), 468–472.
- [33] SUGIURA, M. *Unitary Representations and Harmonic Analysis: An Introduction*. North Holland, 1990.
- [34] THALLER, B. Visualizing the kinematics of relativistic wave packets. arXiv:quant-ph/0409079 (2004)
- [35] THALLER, B. *Advanced visual quantum mechanics*. (Springer Verlag, Heidelberg) (2005)
- [36] TRAPANI, S., AND NAVAZA, J. Calculation of spherical harmonics and Wigner  $d$  functions by FFT. Applications to fast rotational matching in molecular replacement and implementation into *AMoRe*. *Acta Cryst. A* *62* (2006), 262–269.
- [37] TRAUTMAN, A. Connections and the Dirac operator on spinor bundles. *J. Geom. Phys.* *58*, 2 (2008), 238–252.
- [38] TWORZYDŁO, J., GROTH, C. W., AND BEENAKKER, C. W. J. Finite difference method for transport properties of mass-less Dirac fermions. *Phys. Rev. B* *78* (Dec 2008), 235438.
- [39] VOZMEDIANO, M., KATSNELSON, M., AND GUINEA, F. Gauge fields in graphene. *Physics Reports* *496*, 4-5 (2010), 109 – 148.

DEPARTMENT OF MATHEMATICS AND STATISTICS, UNIVERSITY OF OTAGO, PO BOX 56, DUNEDIN 9010, NEW ZEALAND  
*E-mail address:* fbeyer@maths.otago.ac.nz

DEPARTMENT OF MATHEMATICS AND STATISTICS, UNIVERSITY OF OTAGO, PO BOX 56, DUNEDIN 9010, NEW ZEALAND  
*E-mail address:* bdaszuta@maths.otago.ac.nz

DEPARTMENT OF MATHEMATICS AND STATISTICS, UNIVERSITY OF OTAGO, PO BOX 56, DUNEDIN 9010, NEW ZEALAND  
*E-mail address:* joergf@maths.otago.ac.nz